



1 Palaeo-environmental evolution of Central Asia during the Cenozoic: New insights from
2 the continental sedimentary archive of the Valley of Lakes (Mongolia)

3

4 Andre Baldermann^{1*}, Oliver Wasser¹, Elshan Abdullayev^{2,3}, Stefano Bernasconi⁴, Stefan
5 Löhr⁵, Klaus Wemmer⁶, Werner E. Piller⁷, Maxim Rudmin⁸ and Sylvain Richoz⁹

6

7 ¹Institute of Applied Geosciences, Graz University of Technology, NAWI Graz Geocenter, Graz,
8 Austria; baldermann@tugraz.at; oliver.wasser@student.tugraz.at

9 ²Department of Life Sciences, Khazar University, Baku, Azerbaijan; elabdulla3@gmail.com

10 ³Department of Geoscience, French-Azerbaijani University (UFAZ), Baku, Azerbaijan;
11 elabdulla3@gmail.com

12 ⁴Geological Institute, ETH Zurich, Zurich, Switzerland; stefano.bernasconi@erdw.ethz.ch

13 ⁵Department of Earth and Environmental Sciences, Macquarie University, Sydney, Australia;
14 stefan.loehr@mq.edu.au

15 ⁶Geoscience Centre (GZG), University of Göttingen, Göttingen, Germany; kwemmer@gwdg.de

16 ⁷Institute of Earth Sciences, University of Graz, NAWI Graz Geocenter, Graz, Austria;
17 werner.piller@uni-graz.at

18 ⁸Division of Geology, Tomsk Polytechnic University, Tomsk, Russia; rudminma@tpu.ru

19 ⁹Department of Geology, University of Lund, Lund, Sweden; sylvain.richoz@geol.lu.se

20

21 *Corresponding author: Andre Baldermann

22 Institute of Applied Geosciences, Graz University of Technology, 8010, Graz, Austria

23 Tel: +43 316 873 6850, Fax: +43 316 873 6876; E-mail: baldermann@tugraz.at

24

25 Key Words: Cenozoic climate change; Central Asia; Palaeo-environment; Westerly winds;

26 Hydroclimate; Paleosols



27 **Abstract**

28 The Valley of Lakes basin (Mongolia) contains a unique continental sedimentary archive,
29 suitable for constraining the influence of tectonics and climate change on the aridification of
30 Central Asia in the Cenozoic. We identify the sedimentary provenance, the (post)depositional
31 environment and the palaeo-climate based on sedimentological, petrographical, mineralogical
32 and (isotope) geochemical signatures recorded in authigenic and detrital silicates as well as soil
33 carbonates in a sedimentary succession spanning ~34 to 21 Ma. The depositional setting was
34 characterized by an ephemeral braided river system draining prograding alluvial fans, with
35 episodes of lake, playa or open steppe sedimentation. Metamorphics from the northern adjacent
36 Neoproterozoic to late Proterozoic hinterlands provided a continuous influx of silicate detritus to
37 the basin, as indicated by K-Ar ages of detrital muscovite (~798-728 Ma) and discrimination
38 function analysis. The authigenic clay fraction is dominated by illite-smectite and “hairy” illite
39 (K-Ar ages: ~34-25 Ma), which formed during coupled petrogenesis and precipitation from
40 hydrothermal fluids originating from major basalt flow events (~32-29 Ma and ~29-25 Ma).
41 Changes in hydroclimate are recorded in $\delta^{18}\text{O}$ and $\delta^{13}\text{C}$ profiles of soil carbonates and in silicate
42 mineral weathering patterns, indicating comparatively humid to semi-arid conditions prevailed
43 in the late(st) Eocene, changing into arid conditions in the Oligocene and back to humid to
44 semi-arid conditions in the early Miocene. Aridification steps are indicated at ~34-33 Ma, ~31
45 Ma, ~28 Ma and ~23 Ma and coincide with some episodes of high-latitude ice sheet expansion
46 inferred from marine deep-sea sedimentary records. This suggests long-term variations of the
47 ocean/atmosphere circulation patterns due to $p\text{CO}_2$ fall, re-configurations of ocean gateways
48 and ice-sheet expansion in Antarctica could have impacted the hydroclimate and weathering
49 regime in the basin. We conclude that the aridification in Central Asia was triggered by reduced
50 moisture influx by westerly winds driven by Cenozoic climate forcing and the exhumation of
51 the Tian Shan and Altai mountains and modulate by global climate events.



52 **1. Introduction**

53 The Cenozoic Era (66 Ma to the present day) saw several dramatic changes of the marine and
54 continental ecosystems (e.g., evolution of large plankton feeders such as baleen whales, shift
55 towards cold-water, high nutrient plankton assemblages at high latitude, expansion of terrestrial
56 mammals) major tectonic events (e.g., opening of Southern Hemisphere Oceanic gateways,
57 shift to the 4-layer structure of the modern ocean, collision of the African-Arabian-Eurasian
58 plates, uplift of the Alpine and Himalayan mountain belt) and global climate forcing (e.g.,
59 change from greenhouse to icehouse conditions) (Cerling, 1997; Houben et al., 2013; Norris et
60 al., 2013; Cermeño et al., 2015; Mutz et al., 2018; Komar and Zeebe, 2021). The acceleration
61 of Cenozoic climate cooling started after the Early Eocene Climatic Optimum (EECO; ~52-50
62 Ma), with temperatures ~10-12 °C warmer than the modern deep ocean, followed by the
63 appearance and expansion of the Antarctic ice-sheets after the Eocene-Oligocene Transition
64 (EOT; ~34 Ma) and ultimately culminating in the extensive Northern Hemisphere glaciation
65 of the Pleistocene (~2.6-0.01 Ma; Zachos et al., 2001; Lear et al., 2008; Mudelsee et al., 2014;
66 Abdullayev et al., 2021). This long-term transition in Earth's climate is well documented in
67 marine sedimentary archives, but its impact on the evolution of continental ecosystems remains
68 poorly constrained, mainly because continuous, well preserved terrestrial records are scarce
69 and the responses to climate change in these settings are highly complex, depending on latitude,
70 proximity to coast and mountain ranges, position relative to climatic winds, vegetation etc.
71 (e.g., Caves Rugenstein and Chamberlain, 2018; Baldermann et al., 2020). An exception is the
72 sedimentary archive of the Valley of Lakes (Mongolia), which hosts a ~34-21 Ma record of
73 continental sedimentation in Central Asia. The biostratigraphy and the correlation between
74 different outcrops in this basin are well established based on mammalian communities and
75 gastropod records (Harzhauser et al., 2017), magnetostratigraphy (Sun and Windley, 2015) and
76 radiometric age dating of different basalt horizons (Daxner-Höck et al., 2017), rendering this



77 locality suitable for constraining the links between tectonism and climate change in Central
78 Asia during the Cenozoic. The Eocene to Miocene of Central Asia was characterized by
79 accelerated aridification (Dupont-Nivet et al., 2007; Xiao et al., 2010; Bosboom et al., 2014;
80 Li et al., 2016), expressed as a substantially expanded Gobi Desert relative to today (Guo et
81 al., 2008; Lu et al., 2019) and a sudden turnover in the mammal record (Harzhauser et al., 2016;
82 Barbolini et al., 2020). Several, partially opposing hypotheses have been proposed to explain
83 the aridification of Central Asia, including a combination of orbitally-driven climate forcing,
84 the stepwise retreat of the proto-Paratethys Sea and uplift of the Tibetan Plateau (Pälike et al.,
85 2006; Zhongshi et al., 2007; Li et al., 2020) or a continuous decrease of moisture transport by
86 the westerlies due to exhumation of the Tian Shan and Altai mountains (Caves et al., 2014;
87 Caves et al., 2015; Caves Rugenstein and Chamberlain, 2018). However, the evolution of
88 Central Asia's hydroclimate in the Cenozoic was not a period of continuous aridification;
89 indeed, the climatic conditions in particular in the Oligocene were highly complex and
90 characterized by numerous glacial-interglacial cycles (Xiao et al., 2012). Recently, Richoz et
91 al. (2017) have identified two aridification pulses in Central Asia, in the early and late
92 Oligocene, which they assigned to global climatic events. To date, a correlation of the global
93 marine record with the terrestrial record of Mongolia is barely developed (Harzhauser et al.,
94 2016; Harzhauser et al., 2017; Richoz et al., 2017), which limits our understanding of the
95 relative influences of climate change and regional tectonics on the evolution of hydroclimate
96 and weathering conditions in Central Asia in the Cenozoic.

97 In this contribution, we greatly extend the existing mineralogical and (isotope) geochemical
98 dataset previously reported in Richoz et al. (2017) for the Eocene-Miocene sediments from the
99 Valley of Lakes (Mongolia): K-Ar ages and polytype analysis of detrital and authigenic illitic
100 phases coupled with discrimination function analysis and sedimentological-petrographical-
101 geochemical inspection are used to constrain provenance, palaeo-environmental conditions and



102 post-depositional alteration history of this sedimentary succession. Systematic, coherent
103 changes in the weathering patterns of silicate detritus and pristine $\delta^{18}\text{O}$ and $\delta^{13}\text{C}$ signatures
104 recorded in paleosols carbonates allow us to revise and refine the evolution of hydroclimate
105 and weathering conditions in Central Asia in the Cenozoic.

106

107 **2. Geological framework**

108 The Valley of Lakes is an ESE-WNW striking sedimentary basin with ~500 km extension in
109 largest dimension. It is located in Central Mongolia and bordered by the Khangai mountains in
110 the north and the Gobi Altai mountains in the south (Fig. 1a). The geological super-units in the
111 north of Mongolia contain Neoarchean, Proterozoic and Palaeozoic rocks of the Caledonian
112 orogen as well as late Neoproterozoic to Ordovician (Tuva-Mongol) magmatic arc and related
113 back- and fore-arc intrusions, accretionary wedge sequences and ophiolites (Porter, 2016). The
114 geological super-units in the south are characterized mainly by a Palaeozoic orogen, especially
115 the Kazakh-Mongol magmatic arc, which forms the border between Mongolia and China.
116 These units include mainly Devonian to Carboniferous island arc volcanic rocks, Ordovician
117 to Silurian volcanics, Ordovician to Carboniferous metamorphosed sedimentary sequences and
118 Permo-Carboniferous granitoids (Porter, 2016).

119 Regarding the regional lithostratigraphic context, the northern structural units of the Valley of
120 Lakes basin in the Taastsiin Gol area comprise dominantly fault- and thrust-bounded crystalline
121 basement of Neoarchean to Palaeozoic age (Fig. 1b). These include the Baidrag (high-grade
122 gneisses, charnockites and amphibolites, up to 2.65 Ga old) and the Burdgol zone (metapelites,
123 metapsammities and metacherts, 699 ± 35 Ma) in its southernmost end (Teraoka et al., 1996).
124 Further structural units towards the north are the Bayan Khongor (metamorphosed basic rocks,
125 ophiolites and pelitic schists, 450 Ma), the Dzag (metapelites and metapsammities, 440 ± 22
126 Ma and 395 ± 20 Ma) and the Khangai zone (unmetamorphosed, but tectonically deformed



127 sandstones, mudstones and intercalated olistolith sequences of unspecified Devonian to
128 Carboniferous age) (Teraoka et al., 1996; Höck et al., 1999). All of these zones are intruded by
129 numerous granitoids of variable age (Proterozoic to Cretaceous) and composition (Höck et al.,
130 1999). The major zones located in the south of the Valley of Lakes basin comprise the Baga
131 Bogd, the Ikh Bogd and the Bogd som, which are petrographically indistinguishable from the
132 time-equivalent metasediments and metavolcanics of the Bayan Khongor zone and of the
133 Permian quartzitic conglomerates from the adjacent Mount Ushgoeg (Höck et al., 1999).

134 In the focus of this study are the fossiliferous siliciclastic sediments of the Taatsiin Gol Basin,
135 which record important information about changes in sediment provenance, weathering paths
136 and conditions and palaeo-climate in Central Asia during the Eocene to Miocene. The herein
137 investigated sedimentary sections span the Tsagaan Ovoo Formation (upper Eocene), the
138 Hsanda Gol Formation (Oligocene) and the Loh Formation (lower Miocene). Five sections,
139 namely Taatsiin Gol right (TGR-AB), Taatsiin Gol south (TGR-C), Hsanda Gol (SHG-D),
140 Tatal Gol (TAT-E) and Hotuliin Teeg (HTE), were chosen for this study, because of the well-
141 constrained biostratigraphy at these localities. These sections form an integrated sedimentary
142 succession with a thickness of ~115 m (Richoz et al., 2017). Two prominent stratigraphic
143 marker beds, the basalt I group (32.4–29.1 Ma) and the basalt II group (28.7–24.9 Ma) crop out
144 at ~40–41 m and at ~94–100 m in the sedimentary profile (Daxner-Höck et al., 2017). A younger
145 basalt III group (13.2–12.2 Ma) dates back to the middle Miocene, but is not part of the
146 sedimentary succession investigated here. Further details about the local nomenclature, the
147 investigated profiles, profile correlation and lithostratigraphic relationships are provided in
148 Harzhauser et al. (2017), Daxner-Höck et al. (2017) and Richoz et al. (2017). Due to the
149 complex architecture of the Valley of Lakes basin and adjacent areas, a mixed provenance has
150 been proposed for the basin fill, however, detailed knowledge about the palaeo-depositional
151 environment and source area relationships remain poorly constrained (Höck et al., 1999).



152 3. Materials and Methods

153 3.1 Materials

154 Representative bulk sediment samples (140 in total) were taken from different outcrops, which
155 cover the entire sedimentary succession of the Valley of Lakes from the upper Eocene to the
156 lower Miocene. The layers sampled vary in color, composition, texture, fossil and carbonate
157 content, etc., however, they do not show optical signs of alteration, such as recent surface
158 weathering. Samples for geochemical, isotopic and mineralogical analysis were crushed in a
159 ball mill for 10 min and micronized using a McCrone mill for 8 min, with ethanol addition.
160 Samples with a high clay mineral content based on an initial mineralogical inspection were
161 selected further for an identification of the clay mineral suite, which is defined here as $< 2 \mu\text{m}$
162 size fraction (Rafiei et al., 2020). As for the clay mineral separation, 5 g of the bulk material
163 was reacted with 5 % HCl for 10 min to remove the carbonates, followed by standard Atterberg
164 sedimentation and subsequent collection and drying of the $< 2 \mu\text{m}$ size fraction at 40 °C. Fast
165 acid digestion was used to reduce leaching or dissolution of the clay minerals under acidic
166 conditions (Baldermann et al., 2012). Four samples from the Hsanda Gol Formation with a
167 high amount of illitic phases were used for an illite polytype and K-Ar analysis. To this end,
168 three sub-fractions ($< 1 \mu\text{m}$, 1-2 μm and 2-10 μm) were separated by Atterberg sedimentation,
169 which all represent mixtures of authigenic illitic phases and detrital illite/muscovite.

170

171 3.2 Analytical methods

172 The major, minor and trace element composition of a sub-set of samples (91 in total) was
173 analyzed via a Philips PW2404 wavelength dispersive X-ray fluorescence (XRF) spectrometer.
174 Fine powdered samples (0.8 g) were heated to 1050 °C to remove the volatile components
175 (CO_2 , H_2O , etc.), following determination of the loss on ignition (LOI) by gravimetric analysis.
176 The residuals were fused at 1200 °C using LiBO_2 (4 g) as the fluent agent. The standard glass



177 tablets were analyzed together with a set of USGS standards (analytical error: ± 0.5 wt% for
 178 the major elements; Richoz et al., 2017).

179 Sediment origin and variations in the detrital influx among the different provenance areas were
 180 depicted using discrimination plots calculated on the basis of major oxide compositions (Roser
 181 and Korsch, 1988). The weathering paths and intensities in the source rock areas were assessed
 182 through changes in the weathering indices, such as the chemical index of alteration (CIA), the
 183 chemical index of weathering (CIW) and the plagioclase index of alteration (PIA), which were
 184 calculated based on the major oxide compositions using the following equations (Nesbitt and
 185 Young, 1982; Abdullayev et al., 2021):

$$186 \quad CIA = (Al_2O_3 / (Al_2O_3 + CaO^* + Na_2O + K_2O)) \times 100$$

$$187 \quad CIW = (Al_2O_3 / (Al_2O_3 + CaO^* + Na_2O)) \times 100$$

$$188 \quad PIA = (Al_2O_3 - K_2O) / (Al_2O_3 + CaO^* + Na_2O - K_2O) \times 100,$$

189 where CaO^* denotes the fraction of CaO present in the silicate fraction. CaO^* was calculated
 190 by subtraction of the total CaO content of the bulk sediments (determined by XRF analyses)
 191 from the CaO content associated with carbonate minerals (determined by XRD analyses, see
 192 below). The weathering conditions of the source areas were identified further using $Al_2O_3 -$
 193 $CaO^* + Na_2O - K_2O$ (A-CN-K) ternary diagrams (Nesbitt and Young, 1984).

194 The mineralogical composition of all bulk samples was determined by Rietveld-based analysis
 195 of X-ray diffraction (XRD) patterns recorded on a PANalytical X'Pert PRO diffractometer
 196 (Co-K α ; 40 kV and 40 mA) equipped with a high-speed Scientific X'Celerator detector. The
 197 top loading technique was used for the preparation of randomly oriented samples, which were
 198 examined in the range from 4-85 2θ with 0.008°/ 2θ /s step size and 40 s count time. The
 199 PANalytical X'Pert Highscore Plus software and a pdf-4 database were used for mineral
 200 quantification (analytical error: < 3 wt%; Baldermann et al., 2021). The separated grain size
 201 sub-fractions were X-rayed under identical operational conditions. The amounts of authigenic



(1M and 1M_d polytype) and detrital (2M₁ polytype) illitic phases were calculated using the following equations (Grathoff and Moore, 1996):

$$\%2M_1 = 2.05 + 360 \times A_{(114)}/A_{(2.6 \text{ \AA band})}$$

$$\%1M = 4.98 + 136 \times A_{(-112)}/A_{(2.6 \text{ \AA band})}$$

$$\%1M_d = 100 - \%1M \text{ or } 100 - \%2M_1$$

where A is the area (in cps·2θ) of the polytype-specific hkl-reflections of illite and of the 2.6 Å band, respectively (analytical error: $\sim \pm 5 \%$; Baldermann et al., 2017).

Oriented clay films were prepared for the further characterization of the clay mineral fraction (< 2 μm) using a Phillips PW 1830 diffractometer (Cu-Kα; 40 kV and 30 mA) outfitted with a graphite monochromator and a scintillation counter. The clay films were prepared by mixing 50 mg of clay fraction with 5 mL of deionized water, following ultrasonic treatment in a water bath for 10 min to produce a clay-in-suspension, which was subsequently sucked through a porous ceramic tile of ~4 cm² size (Baldermann et al., 2014). The clay films were examined in the range from 3-30° 2θ with 0.02° 2θ step size and 2 s/step count time, each at air-dry states, after solvation with ethylene glycol (EG) and after heat treatment at 550 °C for 1 h. The proportion of illite layers (%Ilt) in mixed-layered illite-smectite (Ilt-Smc) was calculated based on the position of the 002-reflections obtained from XRD patterns of EG-solvated clay films (d_{EG-002} in Å) following the equation (analytical precision: $\pm 5 \%$; Baldermann et al., 2017):

$$\%Ilt = 60.8 \times d_{EG-002} - 504.5.$$

Illite crystallization ages were calculated through coupled illite polytype and K-Ar analysis carried out on the separated grain size sub-fractions. The K₂O content of these samples was determined in digested aliquots (1M HF and HNO₃ mixture) in duplicate via a BWB-XP flame photometer™ using 1 % CsCl as the ionization buffer and 5 % LiCl as the internal standard. The Ar isotopic composition was analyzed in a stainless steel extraction and purification line connected to a Thermo Scientific ARGUS VI™ noble gas mass spectrometer operated in static



mode at the University of Göttingen (Germany). The radiogenic ^{40}Ar content was measured using the standard isotope dilution method applying a highly enriched ^{38}Ar spike calibrated against the biotite standard HD-B1. K-Ar age calculations were made based on the constants recommended by the IUGS (for details see Wemmer et al., 2011). The grain size sub-fractions are free of K-containing mineral phases other than mica/illite group minerals, which would disturb the radiogenic K-Ar ages.

A scanning electron microscopy (SEM) study was carried out to characterize the mineralogy, chemical composition, microfabrics and alteration patterns of the authigenic and detrital (clay) minerals present in the sediments. Therefore, specimens were prepared on standard SEM stubs, coated with carbon and analyzed using a GEMINI® Zeiss Ultra 55 microscope operated at 5-15 kV of accelerating voltage and equipped with a high efficiency in-lens secondary electron (SE) detector and an EDAX Si(Li)-detector for high-resolution imaging and energy-dispersive X-ray spectrometry (EDX) analysis.

The $\delta^{13}\text{C}$ and $\delta^{18}\text{O}$ isotopic composition of the carbonate fraction was analyzed to constrain the palaeo-climatic trends recorded in the paleosols. In a previous study (Richoz et al., 2017) it was shown that the soil carbonates (calcrete nodules, lenses and crusts) mostly record pristine $\delta^{13}\text{C}$ and $\delta^{18}\text{O}$ isotopic compositions reflective of conditions during their formation and are not influenced by detrital or secondary carbonates, such as calcite spar or dolomite. The samples (139 in total) were reacted with 102 % phosphoric acid at 70 °C in a Kiel II automated reaction system and the liberated CO_2 gas analyzed with a ThermoFinnigan mass spectrometer MAT Delta. The measured $\delta^{13}\text{C}$ and $\delta^{18}\text{O}$ values were corrected against the NBS19 standard and are reported in per mill (‰) relative to the Vienna-PeeDee Belemnite (V-PDB) standard (analytical precision: < 0.05 ‰ for $\delta^{13}\text{C}$ and < 0.1 ‰ for $\delta^{18}\text{O}$; Richoz et al., 2017).



250 **4. Results**

251 4.1 Sediment petrography

252 An integrated lithostratigraphic profile of the investigated sedimentary succession (upper
253 Eocene to lower Miocene) from the Taatsiin Gol region, which is a part of the Valley of Lakes,
254 including the biozonation and some field impressions, is presented in Figure 2.

255 The sediments from the Tsagaan Ovoo Formation (upper Eocene) are dominantly coarse clastic
256 sand and gravel deposits of white-greyish color with embedded clay and silt layers of greyish-
257 yellow-green to reddish-brown color, depending on the Fe content (Richoz et al., 2017). The
258 coarser beds show cross-bedding and are frequently poorly sorted, while the finer layers show
259 trough and planar cross-bedding, lamination, inverse to normal grading, rarely ripples and
260 channel fills, and are better sorted. Roots and plant debris and bioturbation features, such as
261 burrows, indicate local paleosol formation (Richoz et al., 2017).

262 The overlying Hsanda Gol Formation (Oligocene) has a higher fossil content (mainly remains
263 of small mammals) and appears as horizontally bedded and poorly sorted clay to silt layers of
264 brick-red to reddish-brown color with intercalated cross-bedded sandstone beds and minor sand
265 and granule lenses of greyish color (Fig. 2c). Paleosol formation is documented by abundant
266 crypto- to microcrystalline calcite nodules and calcite crusts of centimeter to decimeter size
267 encapsulating soil and plant materials (Fig. 2b; Richoz et al., 2017). These calcrete layers of
268 greyish-white color are partially intergrown with Fe- and Mn-(oxy)hydroxides of orange-
269 greyish-black color. The basalt I and basalt II horizons are exposed at ~40-41 m and at ~94-
270 100 m and interfinger with the sediments from the Hsanda Gol Formation (Fig. 2b,d).

271 The Loh Formation (lower Miocene) comprises generally poorly sorted and structure-less silty-
272 clayey horizons with embedded pebbles and lenses of greyish-white to reddish-brown color as
273 well as trough to planar cross-bedded sand and gravel beds of greenish-yellow-red color, which
274 are deposited in alternate mode. Sedimentary structures seen in the coarser beds include inverse



275 to normal grading, ripple marks, channel and scour fills and overbank fines (Richoz et al.,
 276 2017). Most horizons are highly fossiliferous (remains of small mammals and gastropods) and
 277 show signs of paleosol formation, such as calcite nodules and crusts incorporating plant debris,
 278 and burrow structures (Harzhauser et al., 2017).

279

280 4.2 Bulk and clay mineralogy

281 The mineralogical composition of the Valley of Lakes samples is dominated by quartz (10-55
 282 wt%), illite/muscovite (10-50 wt%), calcite (0-70 wt%), feldspar (5-15 wt%; mainly albite and
 283 plagioclase and minor orthoclase) and hematite (0-10 wt%) (Table S1). XRD analysis identifies
 284 the illite/muscovite as an almost pure illitic phase composed of > 95 % Ilt layers and < 5 %
 285 Smc layers (Fig. S1) with the 1M_d polytype structure dominating (~90-95 % of the total illite
 286 fraction; Fig. S2). The proportions of the 1M and 2M₁ polytype structures of illite do not exceed
 287 ~5-10 % of the total illite fraction. Kaolinite, chlorite (Mg-rich), mixed-layered Ilt-Smc
 288 comprised of ~30-10 % Ilt layers and ~70-90 % Smc layers (Fig. S1) as well as Ti-oxides (rutile
 289 and anatase) represent minor constituents (Fig. S2), accounting altogether for less than ~5 wt%
 290 of the sediments. Trace amounts of zeolite and amphibole (< 5 wt%) are documented between
 291 ~35 and 45 m and between ~90 and 110 m in the sedimentary succession, i.e., adjacent to the
 292 basalt I and II groups. Vermiculite, dolomite, ankerite, anhydrite, halite and pyrite were not
 293 identified in the samples, which contrasts observations made by Höck et al. (1999).
 294 The sediments from the Tsagaan Ovoo Formation have the highest proportions of quartz, illite,
 295 feldspar and hematite and the lowest content of calcite compared to the other two formations,
 296 consistent with less abundant calcrete horizons developed in the upper Eocene sediments (Fig.
 297 3a). The sediments from the Oligocene Hsanda Gol and lower Miocene Loh formations have
 298 highly variable, but on average higher calcite contents than the Tsagaan Ovoo Formation due
 299 to abundant paleosol formation and related lower contents of silicate minerals and hematite



(Fig. 3b,c). The depletion of hematite in these samples argues for a detrital origin and for the precipitation of this mineral phase on silicate detritus during sediment transportation under oxic conditions. No systematic trends in the abundance of the mineral phases was observed across the investigated profile (cf. Table S1).

304

4.3 Microfabrics and illite crystallization ages

A microstructural study of weakly consolidated samples taken from the Hsanda Gol Formation reveals (sub)angular to rounded detrital quartz grains (Fig. S3a), which are partly overgrown by diagenetic quartz cement (Fig. S3b), as well as partially dissolved feldspar grains (Fig. S3c). Calichized areas are cemented by calcite spar, which appears as crypto- to microcrystalline material with aggregate particle sizes in the micrometer to millimeter range (Fig. S3d). All these components are covered or intergrown by fine hematite particles (Fig. S3e), although silt-size hematite grains are also observable. Coarse chlorite flakes as well as tiny, rounded to vermiform kaolinite particles are barely seen (Fig. S3f). Indeed, the clay mineral suite is dominated by two types of illite and one type of Ill-Smc. SEM-EDX analysis suggests the illites have higher contents of Al_2O_3 and K_2O , but lower contents of SiO_2 and Na_2O than the Ill-Smc. The illites occur either as micrometer-sized particles with platy or pseudo-hexagonal forms being evenly dispersed throughout the matrix (type 1: Fig. 4a,c,e,g) or as long (micrometer-scale), but thin laths and fibers, which grow into the open pore space (type 2: Fig. 4b,d,f,g,h). The latter type of illite is often referred to as “hairy illite” (Güven et al., 1980; Rafiei et al., 2020). The Ill-Smc is a nanometer-sized material with flaky to irregular particle forms, which covers detrital grains or grows into the open pore space (type 3: Fig. 4b,d,h).

When viewed together with the results of the illite polytype analysis and measured K-Ar ages (Table 1), all sub-samples represent physical mixtures of detrital $2M_1$ illite/muscovite (type 1), authigenic $1M_d/1M$ illite (type 2) and authigenic $1M_d$ Ill-Smc (type 3). Accordingly, the plot



325 of the proportion of $2M_1$ illite/muscovite against the K-Ar age of a given sub-sample (Fig. 5)
 326 provides individual crystallization ages for the detrital and authigenic illitic phases (Grathoff
 327 and Moore, 1996): The upper intercept of the best-fitting line at 100 % of $2M_1$ reveals the
 328 crystallization age of detrital illite/muscovite, which is 727.6 to 797.9 Ma. The lower intercept
 329 of the best-fitting lines at 100 % of $1M_d + 1M$ gives crystallization ages for the authigenic clay
 330 minerals, which vary between 25.2 and 34.2 Ma.

331

332 4.4 Geochemistry and weathering indices

333 Variations in the major element composition of the samples (Table S2) follow changes in the
 334 abundance of silicate minerals (e.g., quartz, feldspar and clay minerals) relative to calcite and
 335 hematite across the sedimentary succession. No distinct trends among the different formations
 336 are seen, except for a lower CaO content and higher contents of SiO_2 , Al_2O_3 , K_2O , Na_2O , MgO
 337 and Fe_2O_3 , on average, in the Tsagaan Ovoo Formation, compared to the Hsanda Gol and Loh
 338 formations, corroborating the mineralogical and petrographic results (cf. Table S1 and Fig. 3).
 339 Minor amounts of TiO_2 belong to rutile and anatase and traces of MnO and P_2O_5 correspond
 340 to Mn-oxides and apatite. The positive correlations of Cu, Ga, Rb and Zn with Al_2O_3 as well
 341 as Ce, La, Y and Zr with TiO_2 and Sr with CaO point to their association with clay minerals
 342 (i.e., structural incorporation or sorption onto the clay mineral surface), heavy minerals and
 343 carbonate minerals, respectively (Abdullayev et al., 2021). Ba, Co, Cr, Hf, Nb, Ni, Pb, Sc, Th,
 344 V and U are inconspicuous due to lack of correlation with Al_2O_3 and TiO_2 or low concentration
 345 in the samples.

346 The plot of the chemical data in the A-CN-K ternary diagram (Fig. 6) shows the samples fall
 347 within or plot slightly above the compositional range of Post-Archean Australian Shale (PAAS)
 348 and Average Proterozoic Shale (APS) and thus follow the predicted weathering trend for basalt
 349 protoliths and Upper Continental Crust (UCC) rocks (Nesbitt and Young, 1984; Bahlburg and



350 Dobrzinski, 2011). The shift of most of the data toward the K pole of the diagrams indicates
 351 K-metasomatism has affected the chemical composition of the sediments through the growth
 352 of authigenic illite and Ill-Smc (Fedo et al., 1995), consistent with petrographic observations
 353 and clay polytype analyses. The CIA, CIW and PIA values vary from 70-83, 83-97 and 79-96
 354 across the different formations, which averages of 79, 94 and 92 for the Loh Formation and 76,
 355 90 and 88 for both the Hsanda Gol and Tsagaan Ovoo formations, respectively (Table S3).

356

357 4.5 Soil carbonate $\delta^{18}\text{O}$ and $\delta^{13}\text{C}$ isotopic composition

358 The $\delta^{18}\text{O}$ and $\delta^{13}\text{C}$ values of the soil carbonates vary in the range from -11.7 to -0.2 ‰ and -
 359 8.1 to -3.8 ‰ across the sedimentary succession of the Valley of Lakes (Table S4). Six samples
 360 taken close to the basalt I and II groups show comparatively lighter isotope values, -12.9 to -
 361 8.6 ‰ of $\delta^{18}\text{O}$ and -9.4 to -8.3 ‰ of $\delta^{13}\text{C}$, which indicates post-depositional overprinting.
 362 Therefore, these samples are not considered further. A high scatter in $\delta^{18}\text{O}$ values (-9.3 to -0.2
 363 ‰) and relatively light $\delta^{13}\text{C}$ values (-7.5 to -6.4 ‰) are seen in the lower part of the Hsanda
 364 Gol Formation, changing into less fluctuating $\delta^{18}\text{O}$ values (-10.3 to -7.0 ‰) and systematically
 365 heavier $\delta^{13}\text{C}$ values (-7.6 to -3.8 ‰) in the middle and upper part of the Hsanda Gol Formation
 366 until the lower Miocene. Around the series/stage boundary, a gradual shift towards lighter $\delta^{18}\text{O}$
 367 values (-11.7 to -8.6 ‰) and fluctuating, but lighter $\delta^{13}\text{C}$ values (-8.1 to -4.4 ‰) are evident.

368

369 5. Discussion

370 5.1 Sediment provenance

371 The time interval from the Neoproterozoic to the late Permian saw the development of large parts
 372 of the fault- and thrust-bounded crystalline basement of Mongolia. The main lithological units
 373 forming this basement include Neoproterozoic metamorphic rocks and Palaeozoic metasediments
 374 and magmatic rocks, which are all intruded by volcanic and magmatic rocks of various age,



375 composition and provenance (Zorin et al., 1993). This complex architecture and the denudation
376 processes in the Mesozoic, which formed the Valley of Lakes basin and created the present-
377 day regional landscape and relief, are documented in the heavy mineral spectra of the Cenozoic
378 basin fill (Höck et al., 1999): the presence of epidote, amphibole, garnet, rutile, pyroxene,
379 sphene, zircon and tourmaline suggest that a mountainous region in the area of the present-day
380 Khangai mountains were the potential source areas (McLennan et al., 1993). Quartz, pegmatite,
381 granite, siltstone, basalt and carbonate clasts found in the gravel fraction (Höck et al., 1999)
382 are also indicative of a heterogeneous provenance for the Valley of Lakes sediments.

383 The major oxide compositions of the sediments from the Valley of Lakes mainly plot in the
384 “P4-quartzose sedimentary provenance” field and only a few samples plot into the “P1-mafic
385 igneous provenance” field in the Roser and Korsch (1988) discrimination diagram (Fig. 7).
386 This indicates metamorphosed sediments rich in quartz and poor in feldspar and subordinate
387 mafic to intermediate igneous and metamorphic rocks are the source rocks for the Valley of
388 Lakes sediments. These rock types are common to all lithological units exposed in the adjacent
389 lands of the Valley of Lakes (Höck et al., 1999). However, if considering the crystallization
390 ages of the 2M₁ detrital illite/muscovite (727.6 to 797.9 Ma, cf. Fig. 5), a robust assignment to
391 provenance areas in the adjacent northern Burdgol zone and Baidrag zone is possible. The
392 Burdgol zone hosts dominantly metapelites, metapsammities and metacherts, which have an
393 age of 699 ± 35 Ma, as inferred from K-Ar dating of muscovite (Teraoka et al., 1996), which
394 closely matches the detrital illite/muscovite ages measured in the sediments from the Valley of
395 Lakes. The shift towards older ages can be explained by a minor contribution of Neoproterozoic
396 rocks from the nearby Baidrag zone (~2.65 Ga old), which are comprised of high-grade
397 gneisses, charnockites and amphibolites. Both source areas coincide with the heavy mineral
398 spectra and gravel lithologies of the Valley of Lakes sediments (Höck et al., 1999).



399 Assuming the detrital illite/muscovite in the Valley of Lakes sediments is a mixture of eroded,
400 metamorphosed and/or intruded material from both source regions, a relative contribution of
401 $\sim > 95\%$ from the Burd gol zone and $\sim < 5\%$ from the Baidrag zone to the total detrital mica
402 fraction can be calculated. Detrital silicate influx from the northernmost Bayan Khongor zone,
403 Dzag zone and Khangai zone is considered to be unlikely, as these source areas are geologically
404 younger (Ordovician to Cretaceous) (Teraoka et al., 1996). Mixtures of different proportions
405 of detritus from the Burd gol zone and some younger and older material are unlikely as well, as
406 constant source proportions over time would be required to explain the same ages for the four
407 investigated samples. Therefore, the source area relationships of the sediments from the Valley
408 of Lakes are less complex than previously thought with most detritus delivered from the
409 regionally adjacent northern areas located within a 100 km range.

410

411 5.2 Depositional environment

412 The poorly sorted, massive to partly cross-bedded sand and gravel beds of the Tsagaan Ovoo
413 Formation are interpreted as debris flow deposits in alluvial fans, according to the classification
414 of Miall (1996) for fluvial sediments. These were generated during or soon after heavy rainfall
415 events, which caused the water-saturated regolith to move down slope (Hubert and Filipov,
416 1989). The finer, laminated layers with ripple marks, inverse to normal grading and channel
417 fills deposited in-between the coarser clastic beds represent the background sedimentation in
418 the upper Eocene, i.e., braided river deposits developed in close vicinity to propagating alluvial
419 fans (Miall, 1996). Imbrications of pebbles, cobbles and clasts within these beds suggest a
420 palaeo-current direction from north to south (Höck et al. 1999), which is consistent with major
421 sediment source areas in the northern Burd gol Zone. Although we found no petrographic-
422 sedimentological evidence for sediment deposition in a lake or playa environment in the upper
423 Eocene, as previously proposed by Badamgarav (1993) and Daxner-Höck et al. (2017), the



424 scatter in the $\delta^{18}\text{O}$ isotopic composition of the soil carbonates, which has been attributed to
425 varying amounts of evaporation (Richoz et al., 2017), may support this assertion.

426 The poorly sorted, often horizontally bedded and fossiliferous clay-silt-sand(stone) beds of the
427 Hsanda Gol Formation were deposited in a complex environment: the finer beds have likely
428 been developed in ephemeral lakes or braided rivers systems draining proximal alluvial fans,
429 as indicated by the presence of channel sand bodies with basal channel scour lags and cross-
430 bedded sand fill. The sandier beds are interpreted as open steppe deposits, which have been
431 temporarily affected by ephemeral river and playa lake sedimentation (Miall, 1996), as it can
432 be inferred from occasional mud cracks and salt crusts (halite; Höck et al., 1999). On the
433 contrary, Sun and Windley (2015) have proposed an eolian origin for the Oligocene sediments
434 and interpreted them as loess deposits, which were transported by westerly winds, based on
435 REE patterns and comparison with grain size distributions obtained from recent Loess deposits
436 from Kansas (USA) and the Chinese Loess Plateau. Although we cannot exclude long-distance
437 transport and subsequent deposition of dust has contributed to at least a minor proportion to
438 the total basin fill of the Valley of Lakes, we found no petrographic evidence for any aeolian
439 influences, such as ripples, coarsening up laminae or climbing translatent strata, ventifacts,
440 mud curls or even quartz grains with crescentic percussion marks (Kenig, 2006; Li et al., 2020).

441 The lithological variability of the Loh Formation (i.e., poorly sorted and highly fossiliferous
442 clay-silt-sand-gravel beds deposited in alternate mode) can be best explained by a combination
443 of debris flow deposits in alluvial fans (coarse clastic material) and abandoned channel deposits
444 and waning flood sedimentation (fine clastic material) of a shallow, perennial flowing braided
445 river system Miall (1996). Imbrication of gravels and flow structures in the basalt III group still
446 indicate a palaeo-current direction from north to south (Höck et al., 1999), which suggests the
447 Burd gol Zone is the main source area at least up to the upper lower Miocene.



448 5.3 Origin of hairy illite and Ilt-Smc

449 Höck et al. (1999) and Sun and Windley (2015) have proposed an aeolian origin or a coupled
 450 aeolian-fluviatile origin for the finest fraction of the Valley of Lakes sediments, while Richoz
 451 et al. (2017) concluded the finest fraction is authigenic and has been formed during or shortly
 452 after the flows of the different basalt groups. However, in none of the above studies radiometric
 453 ages of the clay fraction have been presented to confirm their assertions. Our XRD and SEM
 454 study shows the clay mineral fraction of the Oligocene Hsanda Gol Formation is dominated by
 455 hairy illite and subordinate flake-shaped Ilt-Smc, which cover detrital grains or grow into the
 456 pore space (Fig. 4). All these features that are typical for authigenic illitic phases (Güven et al.,
 457 1980; Rafiei et al., 2020). The polytype analysis and K-Ar age dating reveal these illitic phases
 458 have been precipitated between 34.2 and 25.2 Ma (Fig. 5), which (within uncertainty) is well
 459 within the documented intrusion ages of the basalt I group (32.4-29.1 Ma) and basalt II group
 460 (28.7-24.9 Ma) (Daxner-Höck et al., 2017) and closely matches the biozonation reported in
 461 Harzhauser et al. (2017).

462 The origin of Ilt-Smc in the Valley of Lakes sediments is difficult to constrain: it could have
 463 been formed during low temperature pedogenesis from smectite or kaolinite precursors of
 464 ‘zero’ age (Huggett et al., 2016), which were deposited due to wind (allochthonous clay source)
 465 or soil water (autochthonous source) action, through a dissolution-(re)precipitation mechanism.
 466 Pedogenic degradation of detrital illitic minerals to produce Ilt-Smc under acidic conditions at
 467 low temperature has also been observed (Meenakshi et al., 2020). Contrary, several published
 468 studies question a low temperature origin of Ilt-Smc in sedimentary successions: Ilt-Smc found
 469 in paleosols from the Illinois Basin was shown to be the alteration product of siliceous parental
 470 phases, which interacted with hydrothermal brines generated during burial diagenesis rather
 471 than of ancient soil formation processes (McIntosh et al., 2020). Środoń (1984) concluded that
 472 smectite and Ilt-Smc phases are relatively stable in surface-near surroundings until the elevated



temperatures of deep diagenesis are reached, which is consistent with slow kinetics of smectite illitization calculated for shallow buried sediments and/or low temperature settings (Cuadros, 2006). In the case of the Valley of Lakes sediments, the relatively low Ill content in Ill-Smc (~10-30 % Ill layers) and the stratigraphic age-progression of the authigenic illitic phases up-section in the sedimentary succession may indicate a pedogenic origin of the Ill-Smc. Contrary to the Ill-Smc, a pedogenic origin of the hairy illite is unlikely, because the formation of this mineral phase requires temperatures well around 100 °C (Güven et al., 1980; Nadeau et al. 1985; Baldermann et al., 2017), which is unrealistic high to occur in a developing soil profile that has experienced a maximum burial depth of only a few hundred meters (Richoz et al., 2017). The high Ill content (> 95 % Ill layers) and the hairy appearance of the illite argue for a formation at elevated temperatures, which likely developed simultaneously or shortly after the prominent and recurrent basalt flows, consistent with a basalt-mediated diagenesis. Under such conditions, pore fluids rich in K⁺, Al³⁺ and silicic acid are generated through the dissolution of unstable components, such as feldspar, which subsequently infiltrated the poorly consolidated (porous) Valley of Lakes sediments, thereby promoting the direct precipitation and growth of hairy illite in open pores (Fig. 4) and/or the hydrothermal alteration of pre-existing pedogenic Ill-Smc to hairy illite (Baldermann et al., 2017). This mechanism is applicable to explain the shift of the chemical data towards the K pole in the A-CN-K ternary diagram (Fig. 6).

491

5.5. Palaeo-climate and weathering conditions

Climatic conditions are a primary control of the intensity and type of terrestrial weathering processes, where humid periods favor chemical weathering and arid periods favor physical weathering (Chamley, 1989). Analogously, hydroclimatic conditions take a key control on the intensity of pedogenic processes, which can be recorded in the $\delta^{13}\text{C}$ and $\delta^{18}\text{O}$ isotopic signature of authigenic carbonates (i.e., calcrete in paleosols), where wetter conditions favor an excursion



498 towards lighter $\delta^{13}\text{C}$ and $\delta^{18}\text{O}$ values and drier conditions favor an excursion towards heavier
499 $\delta^{13}\text{C}$ and $\delta^{18}\text{O}$ values (Richoz et al., 2017). Hence, variations in chemical weathering indicators
500 (CIA, PIA and CIW) and in the $\delta^{13}\text{C}$ and $\delta^{18}\text{O}$ profiles of soil carbonates across a sedimentary
501 succession can be used to trace and assess fluctuations in the climatic conditions that prevailed
502 in the source areas and in the sedimentary basin at the time of sediment deposition, and during
503 pedogenesis (Nesbitt and Young, 1982; Bahlburg and Dobrzinski, 2011; Fischer-Femal and
504 Bowen, 2020; Kelson et al., 2020; Zamanian et al., 2021). The formation of soil carbonates is
505 a highly complex process that can complicate the interpretation of their $\delta^{13}\text{C}$ and $\delta^{18}\text{O}$ isotopic
506 values (Richoz et al., 2017), as global climatic trends may be overprinted by regional factors,
507 such as contamination with detrital carbonates, dolomitization, meteoric diagenesis, maturation
508 or oxidation of organic matter, dis-equilibrium conditions between atmospheric (or biogenic)
509 CO_2 and soil solution, evaporation, basalt hydrothermalism, etc. (Kaufman and Knoll, 1995;
510 Kent-Corson et al., 2009; Caves et al., 2014; Li et al., 2016; Baldermann et al., 2020; Li et al.,
511 2020). However, if considering that the pristine soil carbonate $\delta^{13}\text{C}$ and $\delta^{18}\text{O}$ isotopic signature
512 is almost well preserved in the Valley of Lakes sediments, their use for palaeo-environmental
513 reconstructions is possible.

514 The analysis of the $\delta^{13}\text{C}$ and $\delta^{18}\text{O}$ isotopic profiles recorded in the soil carbonates from the
515 Valley of Lakes (~34-21 Ma) yielded the following palaeo-climatic trends, which are consistent
516 with inverse shifts seen in the chemical weathering indices (dashed orange lines in Fig. 8), i.e.,
517 periods with increased precipitation coincide with higher chemical weathering indices and vice
518 versa. This inverse relation is a robust recorder of changing humid/arid climatic conditions in
519 an overall arid climate through the Cenozoic in Central Asia, if considering that the source
520 areas providing the silicate detritus have not changed over time in the investigated sedimentary
521 succession. Accordingly, during the late Eocene to the earliest Oligocene comparatively humid
522 to semi-arid climatic conditions prevailed in Central Asia (phase i); biozone A to bottom part



523 of biozone B; ~34-31 Ma), which is followed by an early Oligocene aridification (phase ii);
524 bottom part of biozone B; ~31 Ma) and the establishment of more arid climatic conditions
525 afterwards until the terminal Oligocene (phase iii); upper part of biozone B to biozone C1-D;
526 ~31-23.5 Ma). A shift back towards comparatively humid to semi-arid climatic conditions is
527 evident in the late Oligocene to earliest Miocene (phase iv); transition between biozones C1-D
528 and D; ~23.5-23 Ma), which is followed by the establishment of these conditions in the early
529 Miocene (phase v); biozone D; ~23-21 Ma).

530 Global cooling events established from $\delta^{13}\text{C}$ and $\delta^{18}\text{O}$ isotope records of marine deep-sea
531 sediments (Zachos et al., 2001; Gallagher et al., 2020), such as the Oi-1a/b Glaciation (~34-33
532 Ma) or the Oligocene Glacial Maximum (~28 Ma) are barely recorded in the soil carbonate
533 $\delta^{13}\text{C}$ and $\delta^{18}\text{O}$ isotope profiles. However, they are visible by increases in chemical weathering
534 indices at exactly these time intervals (blue bars and arrows in Fig. 8) and correspond to
535 important faunal turnovers (Harzhauser et al., 2016). The early Oligocene aridification (~31
536 Ma) is seen by an excursion towards heavier isotopic values between ~55 and 60 m in the rock
537 record, but do not correspond to an important faunal turnover (Harzhauser et al., 2016). On the
538 contrary, the Oligocene warming event (~25 Ma), marked by an important extinction of the
539 mammal community, is not seen in the $\delta^{13}\text{C}$ and $\delta^{18}\text{O}$ isotopic profiles. However, in the interval
540 from ~87 to 92 m (upper part of biozone C1) an increase of all chemical weathering indices is
541 evident, which we attribute to strong illitization and local overprinting of the pristine chemical
542 signature of these sediments. The following Mi-1 Glaciation (~23 Ma) records high chemical
543 weathering patterns, but shows the expected excursion towards lighter $\delta^{13}\text{C}$ and $\delta^{18}\text{O}$ isotopic
544 values.

545 The reasons for the Cenozoic climate change are hotly debated in the literature, but a strong
546 decrease in atmospheric pCO_2 (Pagani et al., 2011; Anagnostou et al., 2016), major tectonic
547 events, such as the collision of India with Asia and progressing exhumation of the Himalaya,



548 as well as re-adjustments in oceanic gateway configurations are widely considered to have
549 altered the global ocean/atmosphere circulation patterns (Caves Rugenstein and Chamberlain,
550 2018). This resulted in large-scale shifts in Earth's climate at this time, which expressed, for
551 example, in the formation and expansion of the Antarctica ice-sheets and periods of intensified
552 chemical weathering on land (Zachos et al., 2001, and references therein).

553

554 5.6 Hydroclimate and tectonics evolution in Central Asia

555 The links between the regional tectonic evolution and climate change in Central Asia have been
556 extensively studied over the past decades. Recently, Caves Rugenstein and Chamberlain (2018)
557 have concluded Central Asia has received moisture through the mid-latitude westerlies,
558 maintaining stable semi-arid to arid climatic conditions ever since the early Eocene, based on
559 the analysis of $\delta^{18}\text{O}$ and $\delta^{13}\text{C}$ isotope systematics of more than 7700 terrestrial authigenic
560 carbonate samples from across Asia. On the contrary, southern Tibet, the central Tibetan
561 Plateau, China and India dominantly received southerly monsoonal moisture, favoring more
562 humid climatic conditions in these regions compared to Central Asia (Ingalls et al., 2018;
563 Sandeep et al., 2018). Our data support this viewpoint: consistently higher $\delta^{18}\text{O}$ and $\delta^{13}\text{C}$ values
564 measured for the soil carbonates from the Valley of Lakes (Fig. 8), compared to the surrounding
565 regions, indicate less precipitation and long-term, sustained arid climatic conditions prevailed
566 in the late Eocene until the early Miocene (Cerling and Quade, 1993; Kent-Corson et al., 2009;
567 Takeuchi et al., 2010; Caves et al., 2015; Li et al., 2016; Caves Rugenstein and Chamberlain,
568 2018). An influence of the height and extension of the Tibetan Plateau or the retreat of the
569 Paratethys on the hydroclimate in Central Asia at this time (An et al., 2001; Zhang et al., 2007)
570 is barely documented in the sedimentary record of the Valley of Lakes, but cannot be excluded,
571 which would express in monsoon-dominant environmental pattern and varying amounts of
572 precipitation (Zhongshi et al., 2007).



573 The increase in the $\delta^{13}\text{C}$ values of the soil carbonates in the Oligocene and the decrease in the
574 $\delta^{18}\text{O}$ values in the terminal Oligocene are ultimately linked to coupled effects arising from the
575 Cenozoic global cooling and the uplift of the Tian Shan and Altai from the early Neogene
576 onward, which caused changes in the seasonality and quantity of precipitation (Hendrix et al.,
577 1994; Macaulay et al., 2016; Hellwig et al., 2017; Wang et al., 2020). The resultant effects on
578 the fractionation of $\delta^{18}\text{O}$ and $\delta^{13}\text{C}$ isotopes in soil carbonates are detailed in Caves Rugenstein
579 and Chamberlain (2018), but are directly related to the development and the establishment of
580 the Altai rain shadow front. As a consequence, on the leeward side of the Altai, sustained, long-
581 term drying occurred, which is expressed by systematic changes seen in the isotope profiles
582 and chemical weathering indices (Fig. 8). This aridification led to a concurrent extension of the
583 Gobi Desert, causing shifts and turnovers in mammalian and gastropod assemblages observed
584 in soils of western Mongolia and in the adjacent eastern Valley of Lakes basin at this time
585 (Neubauer et al., 2013; Harzhauser et al., 2017; Barbolini et al., 2020). We conclude the
586 climatic and environmental evolution of Central Asia in the Cenozoic was closely coupled to
587 global climate change, regional tectonic events and adaptations of the circulation pattern of the
588 westerly winds, transporting less moisture to continental Mongolia, which favored
589 aridification.

590

591 **Acknowledgements**

592 The authors acknowledge M. Hierz, J. Jernej, S. Perchthold and A. Wolf (Graz University of
593 Technology) and S. Šimić (Institute for Electron Microscopy and Nanoanalysis and Graz
594 Centre for Electron Microscopy), who assisted us with the preparation and analysis of the
595 samples. R. Quezada-Hinojosa is greatly acknowledged for drawing the lithostratigraphic
596 profile and for providing the oxygen and carbon isotopic data. This research was funded by the
597 NAWI Graz Geocenter (Graz University of Technology). Field work and sample acquisition



598 was supported by the Austrian Science Fund (FWF) via P-23061-N19 to G. Daxner-Höck. We
599 thank our Mongolian and European team members for manifold support during the field work.

600

601 **Author contributions**

602 A.B. wrote the manuscript. W.E.P. carried out field work and collected the samples. O.W. and
603 S.R. provided the mineralogical and geochemical data. E.A. conducted the discriminant
604 function analyses. K.W. provided the K/Ar ages. A.B., S.B., S.L., W.E.P. and S.R.
605 characterized the palaeo-environment and interpreted the stable $\delta^{13}\text{C}$ and $\delta^{18}\text{O}$ isotope records.
606 All authors contributed to the writing of the manuscript.

607

608 **Additional information**

609 Supplementary materials are provided in the electronic appendix to this paper. Requests for
610 materials and correspondence should be addressed to A.B.

611

612 **Competing interests**

613 All authors declare no competing interests.

614

615 **References**

- 616 Abdullayev, E., Baldermann, A., Warr, L.N., Grathoff, G., Taghiyeva, Y., 2021. New
617 constraints on the palaeo-environmental conditions of the Eastern Paratethys: Implications
618 from the Miocene Diatom Suite (Azerbaijan). *Sedimentary Geology*, 411, 105794,
619 10.1016/j.sedgeo.2020.105794.
- 620 An, Z., Kutzbach, J.E., Prell, W.L., Porter, S.C., 2001. Evolution of Asian monsoons and
621 phased uplift of the Himalaya-Tibetan plateau since Late Miocene times. *Nature*, 411, 62-
622 66, 10.1038/35075035.
- 623 Anagnostou, E., John, E.H., Edgar, K.M., Foster, G.L., Ridgwell, A., Inglis, G.N., Pancost,
624 R.D., Lunt, D.J., Pearson, P.N., 2016. Changing atmospheric CO_2 concentration was the
625 primary driver of early Cenozoic climate. *Nature*, 533, 7603, 380-384,
626 10.1038/nature17423.
- 627 Badamgarav, D., 1993. A brief lithology-genetic characteristics of Eocene-Oligocene and
628 Miocene deposits of the Valley of Lakes and Begger depression. In Barsbold, R., and
629 Akhmetiev, M. A. (Eds.). *International Geological Correlation Programme, Project 326*



- 630 Oligocene-Miocene Transitions in the Northern Hemisphere, Excursion Guide-Book
 631 Mongolia: Oligocene-Miocene Boundary in Mongolia, 36-39.
- 632 Bahlburg, H., Dobrzinski, N., 2011. Chapter 6 A review of the Chemical Index of Alteration
 633 (CIA) and its application to the study of Neoproterozoic glacial deposits and climate
 634 transitions. Geological Society, London, Memoirs, 36, 81-92, 10.1144/M36.6.
- 635 Baldermann, A., Grathoff, G.H., Nickel, C., 2012. Micromilieu controlled glauconitization in
 636 fecal pellets at Oker (Central Germany). Clay Minerals, 47, 513-538,
 637 10.1180/claymin.2012.047.4.09.
- 638 Baldermann, A., Reinprecht, V., Dietzel, M., 2021. Chemical weathering and progressing
 639 alteration as possible controlling factors for creeping landslides. Science of the Total
 640 Environment, 778, 146300, 10.1016/j.scitotenv.2021.146300.
- 641 Baldermann, A., Dohrmann, R., Kaufhold, S., Nickel, C., Letofsky-Papst, I., Dietzel, M., 2014.
 642 The Fe-Mg-saponite solid solution series – a hydrothermal synthesis study. Clay Minerals,
 643 49, 391-415, 10.1180/claymin.2014.049.3.04.
- 644 Baldermann, A., Dietzel, M., Mavromatis, V., Mittermayr, F., Warr, L.N., Wemmer, K., 2017.
 645 The role of Fe on the formation and diagenesis of interstratified glauconite-smectite and
 646 illite-smectite: A case study of Upper Cretaceous shallow-water carbonates. Chemical
 647 Geology, 453, 21-34, 10.1016/j.chemgeo.2017.02.008.
- 648 Baldermann, A., Mittermayr, F., Bernasconi, S.M., Dietzel, M., Grengg, C., Hippler, D., Kluge,
 649 T., Leis, A., Lin, K., Wang, X., Zünterl, A., Boch, R., 2020. Fracture dolomite as an archive
 650 of continental palaeo-environmental conditions. Communications Earth & Environment,
 651 1, 35, 10.1038/s43247-020-00040-3.
- 652 Barbolini, N., Woutersen, A., Dupont-Nivet, G., Silvestro, D., Tardif, D., Coster, P.M.C.,
 653 Meijer, N., Chang, C., Zhang, H.-X., Licht, A., Rydin, C., Koutsodendris, A., Han, F.,
 654 Rohrmann, A., Liu, X.-J., Zhang, Y., Donnadieu, Y., Fluteau, F., Ladant, J.-B., Le Hir, G.,
 655 Hoorn, C., 2020. Cenozoic evolution of the steppe-desert biome in Central Asia. Scientific
 656 Advances, 6, 1-16, eabb8227, 10.1126/sciadv.abb8227.
- 657 Bosboom, R., Dupont-Nivet, G., Grothe, A., Brinkhuis, H., Villa, G., Mandic, O., Stoica, M.,
 658 Huang, W., Yang, W., Guo, Z., Krijgsman, W., 2014. Linking Tarim sea retreat (west
 659 China) and Asian aridification in the late Eocene. Basin Research, 26, 621-640.
 660 10.1111/bre.12054.
- 661 Caves, J.K., Sjöström, D.J., Mix, H.T., Winnick, M.J., Chamberlain, C.P., 2014. Aridification
 662 of Central Asia and uplift of the Altai and Hangay Mountains, Mongolia: stable isotope
 663 evidence. American Journal of Sciences, 314, 1171-1201, 10.2475/08.2014.01.
- 664 Caves, J.K., Winnick, M.J., Graham, S.A., Sjöström, D.J., Mulch, A., Chamberlain, C.P., 2015.
 665 Role of the westerlies in Central Asia climate over the Cenozoic. Earth and Planetary
 666 Science Letters, 428, 33-43, 10.1016/j.epsl.2015.07.023.
- 667 Caves Rugenstein, J.K., Chamberlain, C.P., 2018. The evolution of hydroclimate in Asia over
 668 the Cenozoic: A stable-isotope perspective. Earth-Science Reviews, 185, 1129-1156.
 669 10.1016/j.earscirev.2018.09.003.
- 670 Cerling, T.E., 1993. Late Cenozoic Vegetation Change, Atmospheric CO₂, and Tectonics. In:
 671 Ruddiman, W.F. (eds). Tectonic Uplift and Climate Change. Springer, Boston, MA., 313-
 672 327, 10.1007/978-1-4615-5935-1_13.
- 673 Cerling, T., Quade, J., 1993. Stable carbon and oxygen isotopes in soil carbonates. In P. Swart,
 674 K. Lohmann, J. McKenzie and S. Savin (Eds.). Climate Change in Continental Isotopic
 675 Records. American Geophysical Union, Geophysical Monograph 78, 217-231,
 676 10.1029/GM078p0217.
- 677 Cermeño, P., Falkowski, P.G., Romero, O.E., Schaller, M.F., Vallina, S.M., 2015. Continental
 678 erosion and the Cenozoic rise of marine diatoms. Proceedings of the National Academy of
 679 Sciences of the United States of America, 112, 4239-4244, 10.1073/pnas.1412883112.



- 680 Chamley, H., 1989. Clay Formation Through Weathering. In: Clay Sedimentology. Springer,
 681 Berlin, Heidelberg, Germany, 21-50, 10.1007/978-3-642-85916-8_2.
- 682 Cuadros, J., 2006. Modeling of smectite illitization in burial diagenesis environments.
 683 *Geochimica et Cosmochimica Acta*, 70, 4181-4195. 10.1016/j.gca.2006.06.1372.
- 684 Daxner-Höck, G., Badamgarav, D., Barsbold, R., Bayarmaa, B., Erbajeva, M., Göhlich, U.B.,
 685 Harzhauser, M., Höck, V., Höck, E., Ichinnorov, N., Khand, Y., Lopez-Guerrero, P.,
 686 Maridet, O., Neubauer, T., Oliver, A., Piller, W.E., Tsogtbaatar, K., Ziegler, R., 2017.
 687 Oligocene stratigraphy across the Eocene and Miocene boundaries in the Valley of Lakes
 688 (Mongolia). In G. Daxner-Höck and U. Göhlich (Eds.). *The Valley of Lakes in Mongolia,*
 689 *a key area of Cenozoic mammal evolution and stratigraphy. Palaeobiodiversity and*
 690 *Palaeoenvironments*, 97, 1-9, 10.1007/s12549-016-0257-9.
- 691 Dupont-Nivet, G., Krijgsman, W., Langereis, C.G., Abels, H.A., Dai, S., Fang, X.M., 2007.
 692 Tibetan plateau aridification linked to global cooling at the Eocene-Oligocene transition.
 693 *Nature*, 445, 635-638, 10.1038/nature05516.
- 694 Fedo, C.M., Nesbitt, H.W., Young, G.M., 1995. Unraveling the effects of potassium
 695 metasomatism in sedimentary rocks and paleosols, with implications of paleoweathering
 696 conditions and provenance. *Geology*, 23, 921-924, 10.1130/0091-
 697 7613(1995)023<0921:UTEOPM>2.3.CO;2.
- 698 Fischer-Femal, B.J., Bowen, G.J., 2021. Coupled carbon and oxygen isotope model for
 699 pedogenic carbonates. *Geochimica et Cosmochimica Acta*, 294, 126-144,
 700 10.1016/j.gca.2020.10.022.
- 701 Gallagher, S.J., Wade, B., Qianyu, L., Holdgate, G.R., Bown, P., Korasidis, V.A., Scher, H.,
 702 Houben, A.J.P., McGowran, B., Allan, T., 2020. Eocene to Oligocene high paleolatitude
 703 neritic record of Oi-1 glaciation in the Otway Basin southeast Australia. *Global and*
 704 *Planetary Change*, 191, 103218, 10.1016/j.gloplacha.2020.103218.
- 705 Grathoff, G.H., Moore, D.M., 1996. Illite Polytype Quantification Using Wildfire© Calculated
 706 X-Ray Diffraction Patterns. *Clays and Clay Minerals*, 44, 835-842,
 707 10.1346/CCMN.1996.0440615.
- 708 Guo, Z.T., Sun, B., Zhang, Z.S., Peng, S.Z., Xiao, G.Q., Ge, J.Y., Hao, Q.Z., Qiao, Y.S., Liang,
 709 M.Y., Liu, J.F., Yin, Q.Z., Wei, J.J., 2008. A major reorganization of Asian climate by the
 710 early Miocene. *Climate of the Past*, 4, 153-174, 10.5194/cp-4-153-2008.
- 711 Güven, N., Hower, W.F., Davies, D.K., 1980. Nature of authigenic illites in sandstone
 712 reservoirs. *Journal of Sedimentary Research*, 50, 761-766, 10.1306/212F7ADB-2B24-
 713 11D7-8648000102C1865D.
- 714 Harzhauser, M., Daxner-Höck, G., López-Guerrero, P., Maridet, O., Oliver, A., Piller, W.E.,
 715 Richoz, S., Erbajeva, M.A., Göhlich, U.B., 2016. The stepwise onset of the Icehouse world
 716 and its impact on Oligocene-Miocene Central Asian mammal communities. *Science*
 717 *Reports*, 6, 36169, 10.1038/srep36169.
- 718 Harzhauser, M., Daxner-Höck, G., Erbajeva, M.A., López-Guerrero, P., Maridet, O., Oliver,
 719 A., Piller, W.E., Göhlich, U.B., Ziegler, R., 2017. Oligocene and early Miocene
 720 biostratigraphy of the Valley of Lakes in Mongolia. In G. Daxner-Höck and U. Göhlich
 721 (Eds.). *The Valley of Lakes in Mongolia, a key area of Cenozoic mammal evolution and*
 722 *stratigraphy. Palaeobiodiversity and Palaeoenvironments*, 97, 1-9, 10.1007/s12549-016-
 723 0264-x.
- 724 Hellwig, A., Voigt, S., Mulch, A., Frisch, K., Bartenstein, A., Pross, J., Gerdes, A., Voigt, T.,
 725 2017. Late Oligocene–early Miocene humidity change recorded in terrestrial sequences in
 726 the Ili Basin (south-eastern Kazakhstan, Central Asia). *Sedimentology*, 65, 517-539,
 727 10.1111/sed.12390.



- Hendrix, M., Dumitru, T., Graham, S., 1994. Late Oligocene-early Miocene unroofing in the Chinese Tian Shan: An early effect of the India-Asia collision. *Geology*, 22, 487-490, 10.1130/0091-7613(1994)022<0487.
- Höck, V., Daxner-Höck, G., Schmid, H.P., Badamgarav, D., Frank, W., Furtmüller, G., Montag, O., Barsbold, R., Khand, Y., Sodov, J., 1999. Oligocene-Miocene sediments, fossils and basalt from the Valley of Lakes (Central Mongolia) – an integrated study. *Mitteilungen der Österreichischen Mineralogischen Gesellschaft*, 90, 83-125.
- Houben, A.J.P., Bijl, P.K., Pross, J., Bohaty, S.M., Passchier, S., Stickley, C.E., Röhl, U., Sugisaki, S., Tauxe, L., van de Flierdt, T., Olney, M., Sangiorgi, F., Sluijs, A., Escutia, C., Brinkhuis, H. et al., 2013. Reorganization of Southern Ocean plankton ecosystem at the onset of Antarctic glaciation. *Science*, 340, 341-344, 10.1126/science.1223646.
- Hubert, J.F., Filipov, A.J., 1989. Debris-flow deposits in alluvial fans on the west flank of the White Mountains, Owens Valley, California, U.S.A. *Sedimentary Geology*, 61, 177-205, 10.1016/0037-0738(89)90057-2.
- Huggett, J., Cuadros, J., Gale, A.S., Wray, D., Adetunji, J., 2016. Low temperature, authigenic illite and carbonates in a mixed dolomite-clastic lagoonal and pedogenic setting, Spanish Central System, Spain. *Applied Clay Science*, 132-133, 296-312, 10.1016/j.clay.2016.06.016.
- Ingalls, M., Rowley, D.B., Olack, G., Currie, B.S., Li, S., Schmidt, J.L., Tremblay, M.M., Polissar, P.J., Shuster, D.L., Lin, D., Colman, A.S., 2018. Paleocene to Pliocene high elevation of southern Tibet: Implications for tectonic models of India-Asia collision, Cenozoic climate, and geochemical weathering. *Bulletin of the Geological Society of America*, 130, 307-330, 10.1130/B31723.1.
- Kaufman, A.J., Knoll, A.H., 1995. Neoproterozoic variations in the C-isotopic composition of seawater: stratigraphic and biogeochemical implications. *Precambrian Research*, 73, 27-49, 10.1016/0301-9268(94)00070-8.
- Kelson, J.R., Huntington, K.W., Breecker, D.O., Burgener, L.K., Gallagher, T.M., Hoke, G.D., Petersen, S.V., 2020. A proxy for all seasons? A synthesis of clumped isotope data from Holocene soil carbonates. *Quaternary Science Reviews*, 234, 106259, 10.1016/j.quascirev.2020.106259.
- Kenig, K., 2006. Surface microtextures of quartz grains from Vistulian loesses from selected profiles of Poland and some other countries. *Quaternary International*, 152-153, 118-135, 10.1016/j.quaint.2005.12.015.
- Kent-Corson, M.L., Ritts, B.D., Zhuang, G., Bovet, P.M., Graham, S.A., Chamberlain, C.P., 2009. Stable isotopic constraints on the tectonic, topographic, and climatic evolution of the northern margin of the Tibetan Plateau. *Earth and Planetary Science Letters*, 282, 158-166, 10.1016/j.epsl.2009.03.011.
- Komar, N., Zeebe, R.E., 2021. Reconciling atmospheric CO₂, weathering, and calcite compensation depth across the Cenozoic. *Science Advances*, 7, 1-7, eabd4876, 10.1126/sciadv.abd4876.
- Lear, C.H., Bailey, T.R., Pearson, P.N., Coxall, H.K., Rosenthal, Y., 2008. Cooling and ice growth across the Eocene-Oligocene transition. *Geology*, 36, 251-254, 10.1130/G24584A.1.
- Li, B., Sun, D., Wang, X., Zhang, Y., Hu, W., Wang, F., Li, Z., Ma, Z., Liang, B., 2016. $\delta^{18}\text{O}$ and $\delta^{13}\text{C}$ records from a Cenozoic sedimentary sequence in the Lanzhou Basin, Northwestern China: implications for palaeoenvironmental and palaeoecological changes. *Journal of Asian Earth Sciences*, 125, 22-36, 10.1016/j.jseas.2016.05.010.
- Li, H., Liu, X., Tripathi, A., Feng, S., Elliott, B., Whicker, C., Arnold, A., Kelley, A.M., 2020. Factors controlling the oxygen isotopic composition of lacustrine authigenic carbonates in



- 777 Western China: implications for paleoclimate reconstructions 10, 16370, 10.1038/s41598-
 778 020-73422-4.
- 779 Li, Z., Yu, X., Dong, S., Chen, Q., Zhang, C., 2020. Microtextural features on quartz grains
 780 from eolian sands in a subaqueous sedimentary environment: A case study in the hinterland
 781 of the Badain Jaran Desert, Northwest China. *Aeolian Research*, 43, 100573,
 782 10.1016/j.aeolia.2020.100573.
- 783 Lu, H., Wang, X., Wang, X., Chang, X., Zhang, H., Xu, Z., Zhang, W., Wei, H., Zhang, X.,
 784 Yi, S., Zhang, W., Feng, H., Wang, Y., Wang, Y., Han, Z., 2019. Formation and evolution
 785 of Gobi Desert in central and eastern Asia. *Earth-Science Reviews*, 194, 251-263,
 786 10.1016/j.earscirev.2019.04.014.
- 787 Macaulay, E.A., Sobel, E.R., Mikolaichuk, A., Wack, M., Gilder, S.A., Mulch, A., Fortuna,
 788 A.B., Hynek, S., Apayarov, F., 2016. The sedimentary record of the Issyk Kul basin,
 789 Kyrgyzstan: climatic and tectonic inferences. *Basin Research*, 28, 57-80,
 790 10.1111/bre.12098.
- 791 McIntosh, J.A., Tabor, N.J., Rosenau, A.A., 2020. Mixed-Layer Illite-Smectite in
 792 Pennsylvanian-Aged Paleosols: Assessing Sources of Illitization in the Illinois Basin.
 793 *Minerals*, 11, 108, 10.3390/min11020108.
- 794 McLennan, S.M., 1993. Weathering and Global Denudation. *The Journal of Geology*, 101,
 795 100th Anniversary Symposium: Evolution of the Earth's Surface, 295-303,
 796 <https://www.jstor.org/stable/30081153>.
- 797 Meenakshi, Shrivastava, J.P., Chandra, R., 2020. Pedogenically degenerated illite and chlorite
 798 lattices aid to palaeoclimatic reconstruction for chronologically constrained (8–130 ka)
 799 loess-palaeosols of Dilpur Formation, Kashmir, India. *Geoscience Frontiers*, 11, 1353-
 800 1367, 10.1016/j.gsf.2019.11.007.
- 801 Miall, A.D., 1996. *The geology of fluvial deposits*. Berlin, Germany, Springer, 1-582,
 802 10.1007/978-3-662-03237-4.
- 803 Mudelsee, M., Bickert, T., Lear, C.H., Lohmann, G., 2014. Cenozoic climate changes: A
 804 review based on time series analysis of marine benthic $\delta^{18}\text{O}$ records. *Reviews of*
 805 *Geophysics*, 52, 333-374, 10.1002/2013RG000440.
- 806 Mutz, S.G., Ehlers, T.A., Werner, M., Lohmann, G., Stepanek, C., Li, J., 2018. Estimates of
 807 late Cenozoic climate change relevant to Earth surface processes in tectonically active
 808 orogens. *Earth Surf. Dynam.*, 6, 271-301, 10.5194/esurf-6-271-2018.
- 809 Nadeau, P.H., Wilson, M.J., McHardy, W.J., Tait, J.M., 1985. The conversion of smectite to
 810 illite during diagenesis: evidence from some illitic clays from bentonites and sandstones.
 811 *Mineralogical Magazine*, 49, 393-400, 10.1180/minmag.1985.049.352.10.
- 812 Neubauer, T.A., Harzhauser, M., Daxner-Höck, G., Piller, W.E., 2013. New data on the
 813 terrestrial gastropods from the Oligocene-Miocene transition in the Valley of Lakes,
 814 Central Mongolia. *Paleontological Journal*, 47, 374-385, 10.1134/S003103011304014X.
- 815 Nesbitt, H.W., Young, G.M., 1982. Early Proterozoic climate and plate motions inferred from
 816 major element chemistry of lutites. *Nature*, 299, 715-717, 10.1038/299715a0.
- 817 Nesbitt, H.W., Young, G.M., 1984. Prediction of some weathering trends of plutonic and
 818 volcanic rocks based on thermodynamic and kinetic considerations. *Geochimica et*
 819 *Cosmochimica Acta*, 48, 1523-1534, 10.1016/0016-7037(84)90408-3.
- 820 Norris, R., Turner, S.K., Hull, P.M., Ridgwell, A., 2013. Marine Ecosystem Responses to
 821 Cenozoic Global Change. *Science*, 341, 492-498, 10.1126/science.1240543.
- 822 Pagani, M., Huber, M., Liu, Z., Bohaty, S.M., Henderiks, J., Sijp, W.P., Krishnan, S., DeConto,
 823 R.M., 2011. The Role of Carbon Dioxide During the Onset of Antarctic Glaciation.
 824 *Science*, 334, 6060, 1261-1264, 10.1126/science.1203909.



- 825 Pälike, H., Norris, R.D., Herrle, J.O., Wilson, P.A., Coxall, H.K., Lear, C., H., Shackleton, N.J.,
 826 Tripathi, A.K., Wade, B.S., 2006. The heartbeat of the Oligocene climate system. *Science*,
 827 314, 1894-1898, 10.1126/science.1133822.
- 828 Porter, T.M., 2016. The geology, structure and mineralisation of the Oyu Tolgoi porphyry
 829 copper-gold-molybdenum deposits, Mongolia: A review. *Geoscience Frontiers*, 7, 375-
 830 407, 10.1016/j.gsf.2015.08.003.
- 831 Rafiei, M., Löhr, S., Baldermann, A., Webster, R., Kong, C., 2020. Quantitative petrographic
 832 differentiation of detrital vs diagenetic clay minerals in marine sedimentary sequences:
 833 Implications for the rise of biotic soils. *Precambrian Research*, 350, 105948,
 834 10.1016/j.precamres.2020.105948.
- 835 Richoz, S., Baldermann, A., Frauwallner, A., Harzhauser, M., Daxner-Höck, G., Klammer, D.,
 836 Piller, W.E., 2017. Geochemistry and mineralogy of the Oligo-Miocene sediments of the
 837 Valley of Lakes, Mongolia. *Palaeobiodiversity and Palaeoenvironments*, 97, 233-258,
 838 10.1007/s12549-016-0268-6.
- 839 Roser, B.P., Korsch, R.J., 1988. Provenance signatures of sandstone-mudstone suites
 840 determined using discriminant function analysis of major-element data. *Chemical*
 841 *Geology*, 67, 119-139, 10.1016/0009-2541(88)90010-1.
- 842 Sandeep, S., Ajayamohan, R.S., Boos, W.R., Sabin, T.P., Praveen, V., 2018. Decline and
 843 poleward shift in Indian summer monsoon synoptic activity in a warming climate.
 844 *Proceedings of the National Academy of Sciences of the United States of America*, 115,
 845 2681-2686, 10.1073/pnas.1709031115.
- 846 Środoń, J., 1984. Mixed-layer illite-smectite in low-temperature diagenesis: data from the
 847 Miocene of the Carpathian Foredeep. *Clay Minerals*, 19, 205-215,
 848 10.1180/claymin.1984.019.2.07.
- 849 Sun, J., Windley, B.F., 2015. Onset of aridification by 34 Ma across the Eocene-Oligocene
 850 transition in Central Asia. *Geology*, 11, 1015-1018, 10.1130/G37165.1.
- 851 Takeuchi, A., Hren, M.T., Smith, S.V., Chamberlain, C.P., Larson, P.B., 2010. Pedogenic
 852 carbonate carbon isotopic constraints on paleoprecipitation: Evolution of desert in the
 853 Pacific Northwest, USA, in response to topographic development of the Cascade Range.
 854 *Chemical Geology*, 277, 323-335. 10.1016/j.chemgeo.2010.08.015.
- 855 Teraoka, Y., Suzuki, M., Tungalag, F., Ichinnorov, N., Sakamaki, Y., 1996. Tectonic
 856 framework of the Bayankhongor area, west Mongolia. *Bulletin of the Geological Survey*
 857 *of Japan*, 47, 447-455,
- 858 Wang, X., Carrapa, B., Sun, Y., Dettman, D.L., Chapman, J.B., Rugenstein, J.K.C., Clementz,
 859 M.T., DeCelles, P.G., Wang, M., Chen, J., Quade, J., Wang, F., Li, Z., Oimuhammadzoda,
 860 I., Gadoev, M., Lohmann, G., Zhang, X., Chen, F., 2020. The role of the westerlies and
 861 orography in Asian hydroclimate since the late Oligocene. *Geology*, 48, 728-732.
 862 10.1017/qua.2020.109.
- 863 Wemmer, K., Steenken, A., Müller, S., de Luchi, M.G.L., Siegesmund, S., 2011. The tectonic
 864 significance of K/Ar illite fine-fraction ages from the San Luis formation (Eastern Sierras
 865 Pampeanas, Argentina). *International Journal of Earth Sciences*, 100, 659-669,
 866 10.1007/s00531-010-0629-8.
- 867 Xiao, G.Q., Abels, H.A., Yao, Z.Q., Dupont-Nivet, G., Hilgen, F.J., 2010. Asian aridification
 868 linked to the first step of the Eocene-Oligocene climate Transition (EOT) in obliquity-
 869 dominated terrestrial records (Xining Basin, China). *Climate of the Past*, 6, 501-513,
 870 10.5194/cp-6-501-2010.
- 871 Xiao, G., Zong, K., Li, G., Hu, Z., Dupont-Nivet, G., Peng, S., Zhang, K., 2012. Spatial and
 872 glacial-interglacial variations in provenance of the Chinese Loess Plateau. *Geophysical*
 873 *Research Letters*, 39, L20715, 10.1029/2012GL053304.



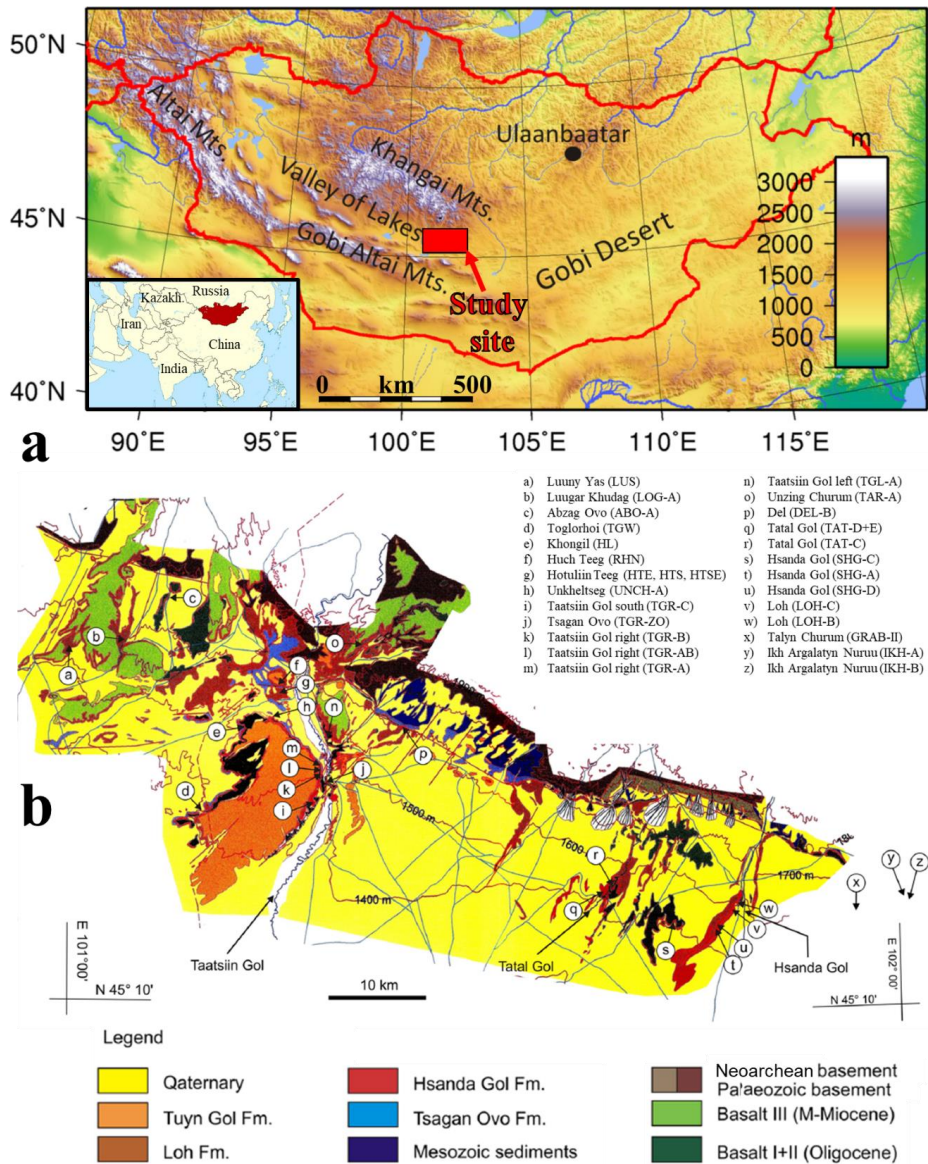
- 874 Zachos, J., Pagani, M., Sloan, L., Thomas, E., Billups, K., 2001. Trends, rhythms, and
 875 aberrations in global climate 65 Ma to present. *Science*, 292, 686-693,
 876 10.1126/science.1059412.
- 877 Zamanian, K., Lechler, A.R., Schauer, A.J., Kuzyakov, Y., Huntington, K.W., 2021. The $\delta^{13}\text{C}$,
 878 $\delta^{18}\text{O}$ and Δ_{47} records in biogenic, pedogenic and geogenic carbonate types from paleosol-
 879 loess sequence and their paleoenvironmental meaning. *Quaternary Research*, 1-17.
 880 10.1017/qua.2020.109.
- 881 Zhang, Z., Wang, H., Guo, Z., Jiang, D., 2007. What triggers the transition of
 882 palaeoenvironmental patterns in China, the Tibetan Plateau uplift or the Paratethys Sea
 883 retreat? *Palaeogeography, Palaeoclimatology, Palaeoecology*, 245, 317-331,
 884 10.1016/j.palaeo.2006.08.003.
- 885 Zhongshi, Z., Wang, H., Guo, Z., Jiang, D., 2007. What triggers the transition of
 886 palaeoenvironmental patterns in China, the Tibetan Plateau uplift or the Paratethys Sea
 887 retreat? *Palaeogeography, Palaeoclimatology, Palaeoecology*, 245, 317-331,
 888 10.1016/j.palaeo.2006.08.003.
- 889 Zorin, Y.A., Belichenko, V.G., Turutanov, E.K., Kozhevnikov, V.M., Ruzhentsev, S.V.,
 890 Dergunov, A.B., Filippova, I.B., Tomurtogoo, O., Arvisbaatar, N., Bayasgalan, T.,
 891 Biambaa, C., Khosbayar, P., 1993. The South Siberia-Central Mongolia transect.
 892 *Tectonophysics*, 225, 361-378, 10.1016/0040-1951(93)90305-4.

895 Figure Captions / Table Captions

896 **Table 1:** Compilation of illite polytype quantification and K-Ar ages of grain size sub-fractions
 897 of sediments collected from (a) TAT section (~90.5 m), (b) TGR-C section (~78.0 m), (c) SHG-
 898 D section (~55.5 m) and (d) TGR-AB section (~35.0 m). The analytical error for the K-Ar age
 899 calculations is given on a 95% confidence level (2σ).

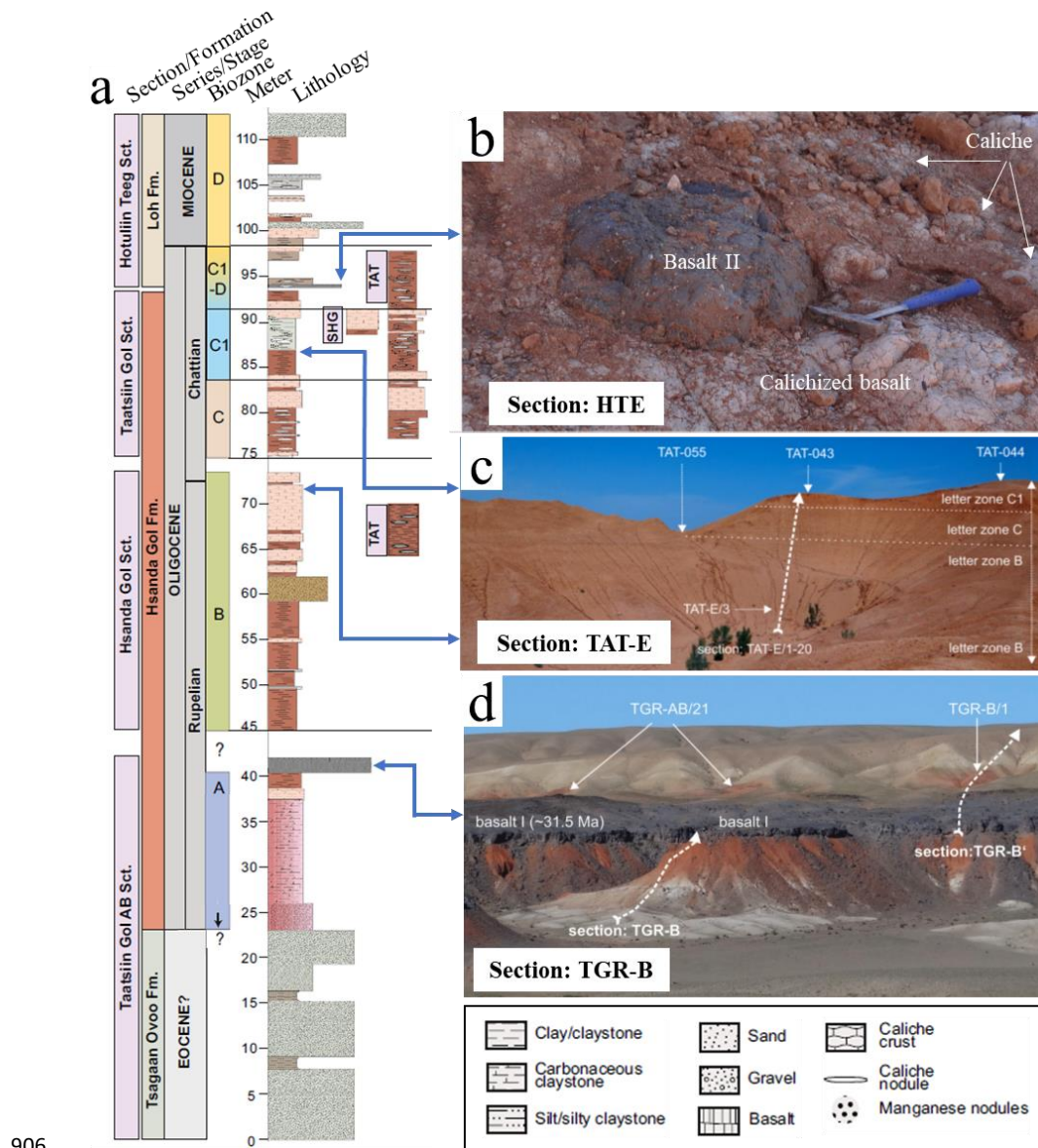
Sample	Size fraction [μm]	$A_{(-112)}$ [cps·20]	1M [%]	$A_{(114)}$ [cps·20]	2M ₁ [%]	1M _d [%]	K ₂ O [wt.%]	$^{40}\text{Ar}^*$ [nl/g] STP	$^{40}\text{Ar}^*$ [%]	Age [Ma]	$\pm 2\text{SD}$ [Ma]
TAT	2-10	-	-	0.054	21	79	2.59	15.45	49.05	176.1	7.1
TAT	1-2	0.006	6	0.040	16	78	2.21	11.58	77.20	155.2	2.6
TAT	< 1	0.012	7	0.023	10	83	3.39	10.75	38.18	95.8	3.2
TGR-C	2-10	-	-	0.038	16	84	2.68	13.98	81.46	155.1	2.9
TGR-C	1-2	-	-	0.031	13	87	3.64	15.80	76.96	129.6	2.4
TGR-C	< 1	0.001	5	0.027	12	95	3.10	12.88	66.83	124.6	1.9
SHG-D	2-10	-	-	0.039	16	84	2.72	14.31	78.74	156.4	2.0
SHG-D	1-2	-	-	0.034	14	86	3.86	15.93	76.09	123.6	3.2
SHG-D	< 1	0.011	6	0.016	8	94	3.49	10.38	70.94	89.9	1.3
TGR-AB	2-10	-	-	0.032	14	86	3.83	17.29	84.05	134.8	3.4
TGR-AB	1-2	-	-	0.027	12	88	3.97	16.63	84.33	125.3	1.8
TGR-AB	< 1	0.032	9	-	0	91	0.64	0.70	10.52	33.9	3.2

900



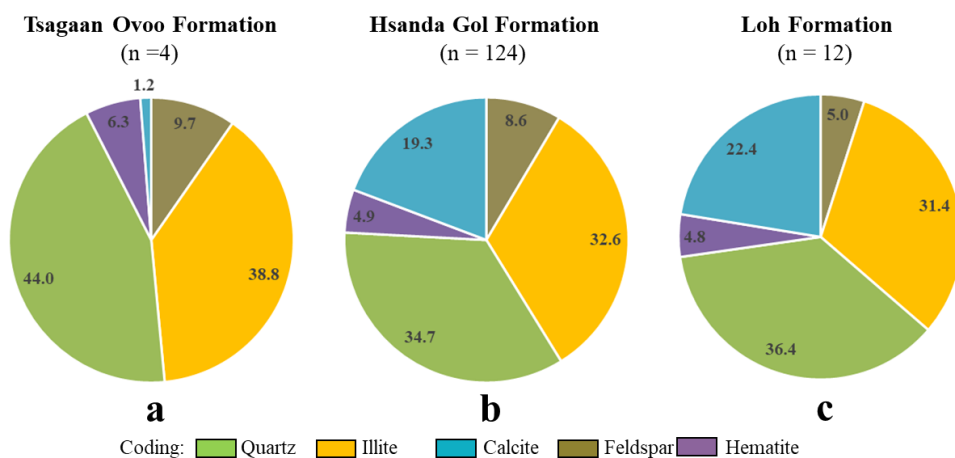
901

902 **Figure 1:** (a) Location of the study site in the Taatsiin Gol region, a part of the Valley of Lakes,
903 in Mongolia (Central Asia). Altitude in meters is indicated on the right. (b) Geological map of
904 the Taatsiin Gol area within the Valley of Lakes with the sampling sites marked in alphabetical
905 order (modified after Daxner-Höck et al., 2017).



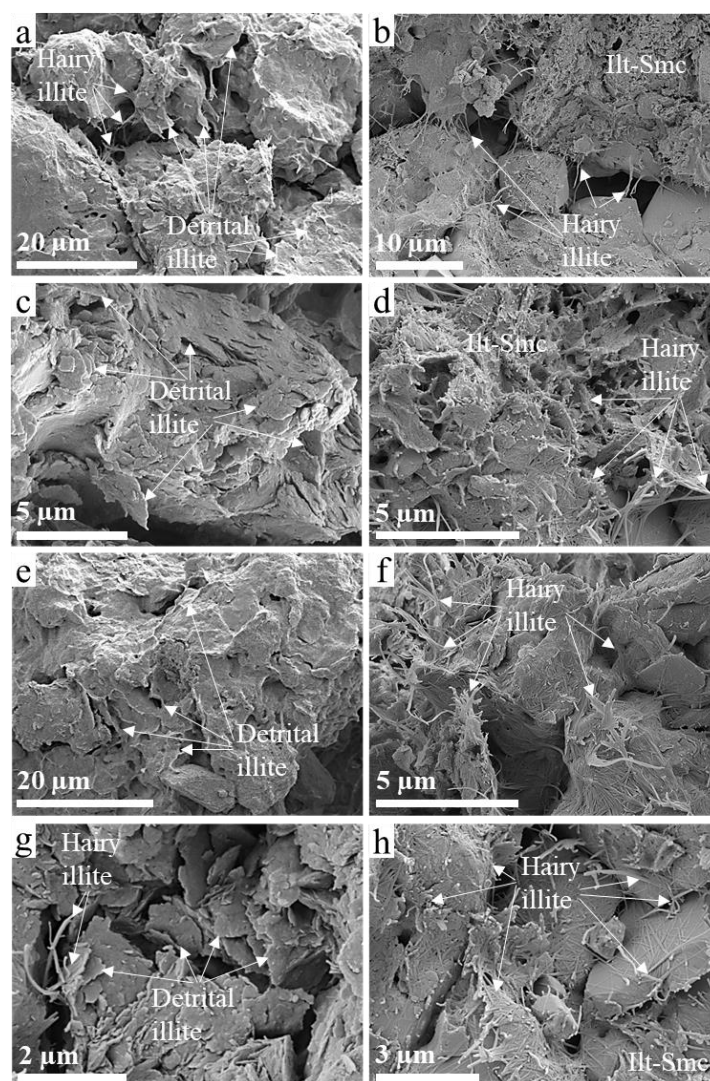
906

907 **Figure 2:** (a) Integrated lithostratigraphic profile of the investigated sedimentary succession
908 from the Taatsiin Gol region, Valley of Lakes (modified after Richoz et al., 2017), with
909 biozonation (modified after Harzhauser et al., 2017). (b-d) Field impressions of the sections
910 Hotuliin Teeg (HTE) with calichized basalt II group, Tatal Gol (TAT-E) sediments and Taatsiin
911 Gol right (TGR-B) section with basalt I group (modified after Daxner-Höck et al., 2017).



912

913 **Figure 3:** Averaged mineralogical composition (in wt%) of the sediments from the (a) upper
 914 Eocene Tsagaan Ovoo Formation, (b) Oligocene Hsanda Gol Formation and (c) lower Miocene
 915 Loh Formation from the Valley of Lakes, determined by XRD analysis.



916

917 **Figure 4:** Secondary electron images of partly calichized and illitized silty to sandy deposits
 918 from the of the Oligocene Hsanda Gol Formation, Valley of Lakes, collected from (a-b) TAT
 919 section (~90.5 m), (c-d) TGR-C section (~78.0 m), (e-f) SHG-D section (~55.5 m) and (g-h)
 920 TGR-AB section (~35.0 m). The detrital illite/muscovite (left panel) occurs as coarse, rounded
 921 or pseudo-hexagonal platelets, whereas authigenic illite-smectite (Ilt-Smc) and hairy illite (right
 922 panel) appear either as fine, flaky to irregular particles or as long, but thin laths and fibers, both
 923 covering detrital grains or growing into the open pores.

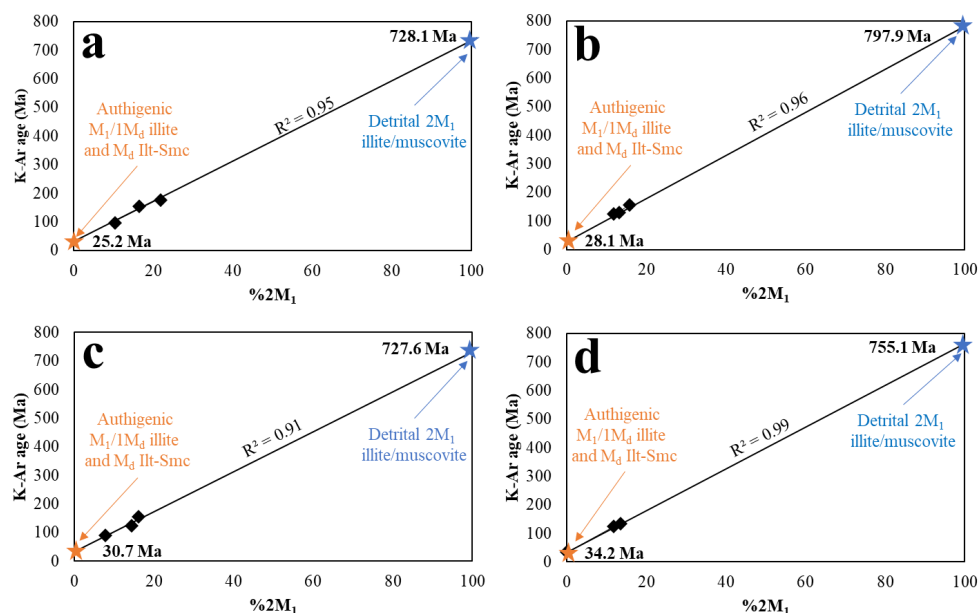
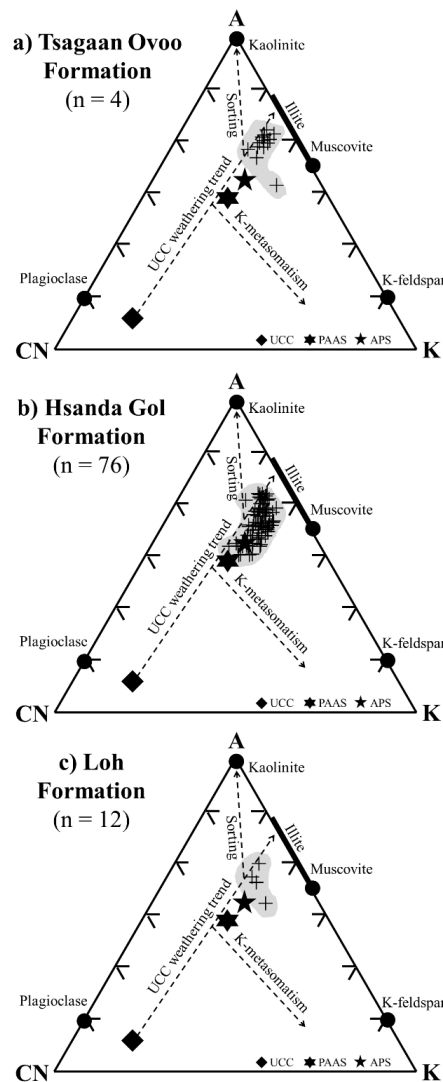
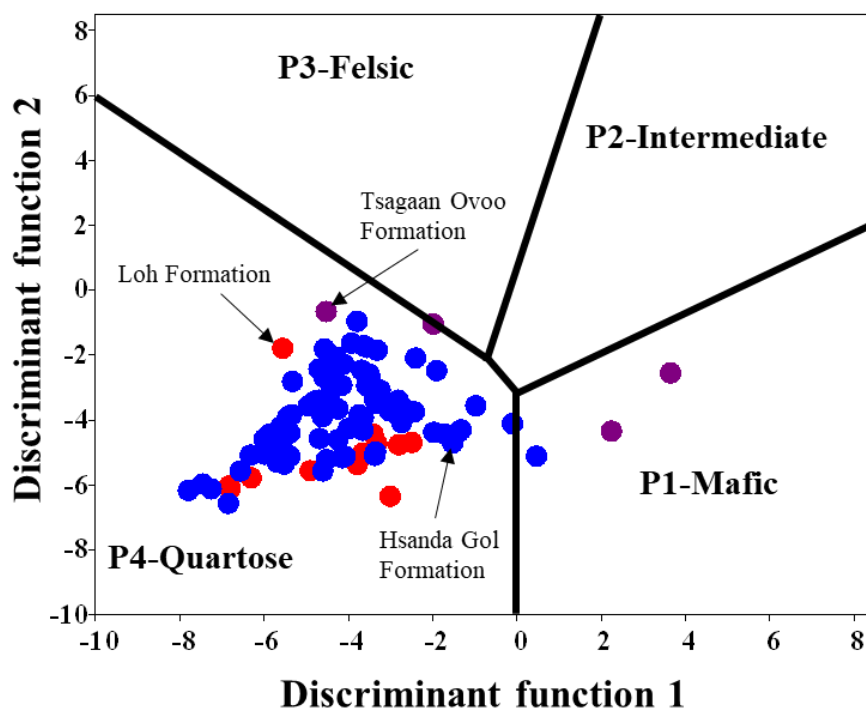


Figure 5: Crystallization ages of detrital 2M₁ illite/muscovite and of authigenic 1M_d/1M illite and illite-smectite (Ilt-Smc) from the Valley of Lakes, calculated for sediments collected from (a) TAT section (~90.5 m), (b) TGR-C section (~78.0 m), (c) SHG-D section (~55.5 m) and (d) TGR-AB section (~35.0 m) using illite polytype quantification and K-Ar age systematics of different grain size sub-fractions (from left to right: < 1 μm, 1-2 μm and 2-10 μm).



930

931 **Figure 6:** Al_2O_3 -($\text{CaO}^*+\text{Na}_2\text{O}$)- K_2O (A-CN-K) ternary diagram of Nesbitt and Young (1984)
932 showing the compositional ranges of sediments from the Valley of Lakes from (a) upper
933 Eocene Tsagaan Ovoo Formation, (b) Oligocene Hsanda Gol Formation and (c) lower Miocene
934 Loh Formation. Note that most samples are shifted to the K pole of the diagram, which indicates
935 a post-depositional enrichment of K_2O due to illitization. The composition of Upper
936 Continental Crust (UCC), Average Proterozoic Shale (APS) and Post-Archean Australian
937 Shale (PAAS) are included for comparison.



938

939 **Figure 7:** Discrimination plot of discriminant function 1 and 2 indicating a narrow provenance

940 range (mainly type P4-quartzose) for the sediments from the Valley of Lakes, Mongolia.

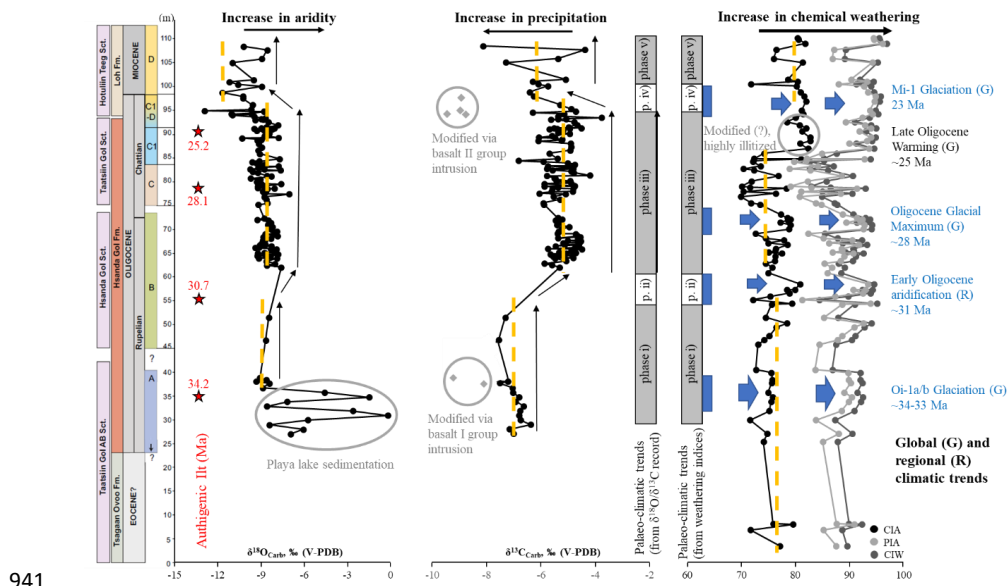


Figure 8: Lithostratigraphic framework of the sediments from the Valley of Lakes (Mongolia, Central Asia) showing the biozonation (modified after Harzhauser et al., 2017) and formation ages of authigenic illitic (Ilt) phases obtained in this study (red asterisks), as well as soil carbonate $\delta^{18}\text{O}$ and $\delta^{13}\text{C}$ isotope profiles and shifts in the silicate mineral-derived chemical weathering indicators. Note that these hydroclimate proxies are inversely correlated and follow long-term trends (indicated by orange dashed lines) in aridification or gain of humidity in this region (indicated by black arrows). Increased chemical weathering degrees (highlighted with blue bars and blue arrows) coincide with glaciation events documented in time-equivalent marine deep-sea deposits (Zachos et al., 2001; Gallagher et al., 2020). Samples and intervals outlined with grey circles are most likely modified due to the flows of the basalt I and II groups or local strong illitization, and are therefore excluded from the palaeo-climatic interpretation.